Abrupt stratospheric vortex weakening associated with North Atlantic anticyclonic wave breaking

Article

Accepted Version

Abrupt stratospheric vortex weakening associated with North Atlantic anticyclonic wave breaking

S. H. Lee[1], A. J. Charlton-Perez[1], J. C. Furtado[2], and S. J. Woolnough[3,1]

[1]Department of Meteorology, University of Reading

[2]School of Meteorology, University of Oklahoma

[3]National Centre for Atmospheric Science, University of Reading

Key Points:

- In early February 2018, forecasts abruptly transitioned from indicating a strong stratospheric polar vortex to sudden stratospheric warming.
- This was due to the predictability of a cyclone in the North Atlantic which was associated with driving an anticyclonic Rossby wave break.
- Similar historical cases show this as a mechanism for weakening the stratospheric polar vortex which can lead to major sudden warmings.

Corresponding author: Simon Lee, `s.h.lee@pgr.reading.ac.uk`

Abstract

The sudden stratospheric warming (SSW) of 12 February 2018 was not forecast by any extended-range model beyond 12 days. From early February, all forecast models that comprise the subseasonal-to-seasonal (S2S) database abruptly transitioned from indicating a strong stratospheric polar vortex (SPV) to a high likelihood of a major SSW. We demonstrate that this forecast evolution was associated with the track and intensity of a cyclone in the north-east Atlantic, with an associated anticyclonic Rossby wave break, which was not well-forecast. The wave break played a pivotal role in building the Ural high, which existing literature has shown was a precursor of the 2018 SSW. The track of the cyclone built an anomalously strong sea-level pressure dipole between Scandinavia and Greenland (termed the S-G dipole) which we use as a diagnostic of the wave break. Forecasts which did not capture the magnitude of this event had the largest errors in the SPV strength and did not show enhanced vertical wave activity. A composite of 49 similarly strong wintertime (November–March) S-G dipoles in reanalysis shows associated anticyclonic wave breaking leading to significantly enhanced vertical wave activity and a weakened SPV in the following days, which occured in 35% of the 15-day periods preceding observed major SSWs. Our results indicate a particular transient trigger for weakening the SPV, complementing existing results on the importance of tropospheric blocking for disruptions to the Northern Hemisphere extratropical stratospheric circulation.

Plain Language Summary

During winter, a large circulation 10-50 km above the pole (known as the stratospheric polar vortex) can influence the day-to-day weather patterns in the troposphere beneath from weeks to months later. Thus, being able to predict the behavior of the stratospheric polar vortex is important for predicting the weather on longer time-frames. In February 2018, the Northern Hemisphere stratospheric polar vortex broke apart in an event known as a sudden stratospheric warming, which was not well-forecast. This event led to unusually cold conditions across Eurasia. In this article we find the poor predictability of the event was due to a poorly forecast weather system in the Atlantic. We also show that this pattern was present in previously observed cases where the stratospheric polar vortex has weakened. Our results demonstrate a trigger mechanism for these extreme events and have implications for our ability to predict the weather at longer ranges.

1 Introduction

The major mid-winter sudden stratospheric warming (SSW) event of 12 February 2018 was the first major SSW since January 2013 (defined as a reversal of the daily-mean 10 hPa 60°N zonal-mean zonal winds (Charlton & Polvani, 2007)), a 5 year gap which was the longest since 1989–1998 according to the SSW Compendium (Butler, Sjoberg, Seidel, & Rosenlof, 2017). It produced a split of the stratospheric polar vortex (SPV) into two smaller vortices. Following the metric of Karpechko, Hitchcock, Peters, and Schneidereit (2017) the event was downward-propagating with the negative phase of the stratospheric Northern Annular Mode (NAM) (Baldwin & Dunkerton, 2001; Thompson & Wallace, 2000) accompanied by a strong and persistent negative tropospheric NAM in the 45 days following the event. The negative tropospheric NAM and associated negative North Atlantic Oscillation (NAO) produced extremely cold conditions across Europe and northern Asia, with a large anticyclone over Scandinavia generating a cold easterly flow (Ferranti, Magnusson, Vitart, & Richardson, 2018). With such a high impact response, the ability to predict the onset of an SSW like in 2018 is of vital importance for sub-seasonal forecasting.

The 2018 SSW was the first to occur following the development of the subseasonal-to-seasonal (S2S) database of extended-range forecasts from 11 international forecast models (Vitart et al., 2017). None of the S2S model forecasts issued at the time indicated a major SSW until early February (Karpechko, Charlton-Perez, Balmaseda, & Vitart, 2018), giving a predictability window less than the medium-range timeframe (∼2 weeks). Although this lies within the window typical of predicting major SSWs (Taguchi, 2014; Tripathi et al., 2016, 2015), S2S model forecasts abruptly transitioned from projecting a strong SPV to a weak SPV/major SSW in late January-early February, with a corresponding transition in forecasts of tropospheric conditions (such as from forecasts of a positive NAO to a negative NAO). Karpechko (2018) showed several SSWs were poorly forecast in ECMWF hindcasts at lead-times beyond 7–10 days, but most were generally associated with a longer-range signal of SSW likelihood.

Specifically for the February 2018 event, Karpechko et al. (2018) examined S2S model forecasts from 1 February onwards and showed a strong relationship between the accuracy of stratospheric wind forecasts and the intensity of an anticyclone over the Urals (named the 'Ural high'). However, they did not assess the longer-term predictability of

the event, the mechanism driving the onset of the Ural high, or its influence on the stratosphere, leaving open questions about the abrupt predictability onset. The Ural high has also been shown to drive SPV variability (Peings, 2019; White et al., 2019) by projecting onto the climatological stationary wave pattern.

Most studies of SSW precursors use a 'top-down' perspective, where the tropospheric features are analyzed in the period preceding observed stratospheric events. These approaches typically discern stationary or longer-lived features through the process of averaging anomalies in the build-up to SSWs. Tropospheric blocking is one such feature (e.g. Colucci & Kelleher, 2015; Garfinkel, Hartmann, & Sassi, 2010; Julian & Labitzke, 1965; Martius, Polvani, & Davies, 2009; Quiroz, 1986). For example, Bao, Tan, Hartmann, and Ceppi (2017) used cluster analysis to assess 500 hPa geopotential height patterns in the month before 37 SSWs in reanalysis, and found the patterns to be associated with linear interference with climatological stationary waves. Kolstad and Charlton-Perez (2011) used reanalysis alongside climate model simulations and found a particularly strong signal for a height anomaly dipole over northern Eurasia preceding 'weak vortex months'. Other studies have considered more transient features associated with specific stratospheric events. Coy, Eckermann, and Hoppel (2009) noted the importance of zonal wavenumbers 4-5 associated with synoptic-scale systems preceding the SSWs of January 2006 and 2003. They implicated tropospheric systems over the North Atlantic and subtropical wave breaking; forecasting experiments showed a realistic SSW only occurred when a North Atlantic weather system was correctly represented in the model. On the other hand, a study of the January 2013 SSW (Coy & Pawson, 2014) suggested a rapidly-deepening cyclone in the North Atlantic played only a minor role, acting as a transient source of vertical wave activity that was not crucial to forcing the event. The authors also remark on the dynamical link between the initial stratospheric vortex state and the track of the cyclone, suggesting a two-way relationship. O'Neill, Oatley, Charlton-Perez, Mitchell, and Jung (2017) demonstrated a link between extratropical tropospheric cyclogenesis occurring at the edge of the SPV and split-type SSWs through a potential vorticity framework. Although mainly focusing on the Southern Hemisphere SSW of 2002 (e.g. Krüger, Naujokat, & Labitzke, 2005), they briefly show a similar mechanism with cyclogenesis over the eastern seaboards of the Northern Hemisphere continents. Most recently, Attard and Lang (2019) approach the problem by looking at the meridional eddy heat flux, and demonstrate the different responses for blocks and 'bomb' cyclones in the

Atlantic and Pacific sectors. They conclude cold-season Atlantic bomb cyclones and Pacific blocks were associated with negative heat flux anomalies (and vice versa) whilst also noting that only a relatively small number of blocks and bombs are actively associated with SSWs.

Thus, there exist both transient and stationary drivers of stratospheric variability (including but not limited to SSWs), the predictability of which plays a role in the onset of SSW prediction. In this study, we provide a dynamical explanation for the abrupt transition in the forecasts of the February 2018 event, building upon existing analysis. We demonstrate that this is a characteristic of historical cases of vortex weakening, rather than unique to the flow configuration driving the 2018 event, through a 'bottom-up' approach (analysing the response of the stratosphere to tropospheric events). Our results have implications for extended-range predictability of SSWs and thus sub-seasonal tropospheric forecasts.

2 Data and Methods

We use forecast data from the European Centre for Medium Range Weather Forecasts (ECMWF) and National Centers for Environmental Prediction (NCEP) models, as these provide a combination of both large ensemble sizes and frequent launch dates - ECMWF launches twice weekly (Tuesday and Thursday) with 51 members, and NCEP launches daily with 16 members. The predictability onset of the SSW was common across all the S2S models (Karpechko et al., 2018), so our analysis is not sensitive to the choice of model. For verification, we use the ECMWF ERA-Interim reanalysis (Dee et al., 2011). The strength of the SPV is defined using the zonal-mean zonal wind at 10 hPa and 60°N ($U10_{60}$). We use 45–75°N meridionally-averaged zonal-mean eddy heat flux (denoted as [v*T*] where the star notation indicates a departure from the zonal-mean, and square brackets indicate a zonally-averaged quantity) at 300 hPa as a proxy for upper-tropospheric wave activity. This is proportional to the vertical component of the Eliassen-Palm flux (Andrews, Holton, & Leovy, 1987). Standardized polar cap (60–90°N) geopotential height anomalies are used as a proxy for the NAM index (Karpechko et al., 2017); the anomalies are inversely proportional to the index. Unless otherwise stated, standardized anomalies are computed with respect to the climatological daily-mean and standard deviation in ERA-Interim. Historical composites use data from January 1979–March 2017 inclusive, and statistical significance is assessed using a bootstrap re-sampling method with

replacement (n = 50,000) for November–March in the period January 1979 to March 2017. Potential vorticity is analyzed on the 315 K isentropic surface in ERA-Interim data and the 320 K isentropic surface in model forecast data as these are the nearest tropospheric levels available in both datasets. All data are re-gridded to 2.5° horizontal resolution for consistency.

3 Results

3.1 Characterizing the Onset of SSW Predictability

To demonstrate the evolution of forecasts of the zonal-mean state, Figure 1 (a, c) shows forecasts of $U10_{60}$ for the first 5 days of the verifying SSW (12–16 February) for all forecasts in which those dates featured. There is an abrupt transition in late January-early February from forecasts of a strong vortex to a weakened vortex or major SSW. In both ECMWF and NCEP systems, the 29 January ensembles showed no members indicating mean easterlies during this period, with a tightly clustered ensemble. The following day, forecasts from NCEP substantially changed, with some members suggesting a mean zonal wind reversal and the entire ensemble forecasting weaker $U10_{60}$ than the 25^{th} percentile of the ensemble from the previous day – a change which also occurred in the 29 January and 1 February ECMWF ensembles. There is also an increase in spread despite the reduced lead-time. Ensemble spread was then much reduced by 5-6 February, a lead-time of only 6-7 days before the major SSW. A similar predictability evolution is found in other S2S models (not shown), indicating this was not related to the ability of certain models to capture the event. Moreover, we see the abrupt transition of vortex strength was associated with an abrupt increase in 300 hPa [v*T*] preceding the wind reversal (Figure 1b and 1d). The increase in forecast heat flux suggests the low predictability of the SSW was dependent on poorly-forecast tropospheric wave-driving, rather than the response of the stratospheric vortex to a wave pulse or the sensitivity of the $U10_{60}$ metric.

To investigate this evolution further, we look at the 29 January and 1 February ensembles from ECMWF, which cover the spread of evolutions from strong vortex to weak vortex (Figure 2). The ensembles systematically diverge after 5 February – with the forecasts from 29 January showing low wave activity and strengthening zonal-mean zonal winds, whilst the opposite is true for forecasts from 1 February. This is an even greater

divergence in zonal wind intensity than day-15 forecasts for the January 2013 SSW shown in Tripathi et al. (2016). Despite the 3 day difference in lead-time, the systematic difference between the two ensembles motivates considering them together to capture the uncertainty. Analysis in the corresponding NCEP ensembles gives similar results (see Figure S1).

Thus, there are two alternative scenarios demonstrated in ensemble forecasts from late January and early February: (a) enhanced vertical wave activity around 5 February leading to SPV weakening, and (b) suppressed wave activity with little subsequent change in SPV strength. In the next section, we discern the tropospheric drivers for these divergent stratospheric evolutions.

3.2 Characterizing Tropospheric Uncertainty

Figure 3 depicts the linear correlation between the mean $U10_{60}$ forecast for 9–11 February (a period where ensemble members either projected a quiescent vortex or strong deceleration, c.f. Figure 2) and the mean sea-level pressure (MSLP) for 3–5 February (i.e., just before the onset of enhanced vertical wave flux). This correlation is calculated in joined ensembles from 29 January to 1 February in NCEP (to increase ensemble sample size and incorporate a larger range of SPV strengths), and 29 January and 1 February in ECMWF; independent calculations (not shown) for the separate ensembles suggest this is not a result of the difference in character of the forecasts or a facet of the differences in lead-time. We average across forecasts initialized during the onset of predictability of the vortex weakening event (c.f. Figure 1) to determine what changed during this window. The results show the strongest correlations between the preceding MSLP field and the strength of the SPV form a dipole between Scandinavia and Greenland. Secondary regions of strong correlation are also located upstream and downstream of the main dipole. The correlation field indicates that ensemble members with lower MSLP over eastern Greenland and higher MSLP over Scandinavia forecast weaker $U10_{60}$. Based on this correlation analysis, we define the Scandinavia-Greenland dipole in MSLP (hereafter, the S-G dipole) to describe the evolution. We calculate this by subtracting the area-average MSLP in a grid box over Scandinavia (60-70°N, 12.5-42.5°E) from that in a grid box over eastern Greenland (72.5-90°N, 2.5-42.5°W). The MSLP in each grid box is cosine-weighted to account for the convergence of meridians at higher latitudes. The two nodes, primarily based on the track of a cyclone and the development of a Scandinavian ridge (see Fig-

ure 4), are shown as black dashed lines in Figure 3. The Ural high, also shown Figure 3, is defined as the area-average MSLP in the grid box 45-60°N, 50-80°E.

To discern the tropospheric drivers of the vertical wave flux, we assess the MSLP evolutions of ECMWF ensemble members from 29 January and 1 February 2018 with the top and bottom 10%-mean 300 hPa [v*T*] for 4–6 February. Results (Figure 4) support the correlation analysis from Figure 3; a cyclone near Iceland on 3 February progresses up the eastern coast of Greenland and deepens to <970 hPa by 5 February in the high-flux members, with a ridge extending from the Azores through Scandinavia, whilst in the low-flux members the cyclone moves south-east towards Europe and weakens without any ridge development. Figure 4c demonstrates the dipole structure; pressures are >20 hPa higher (lower) over Scandinavia (Greenland) in the top 10% versus the bottom 10% heat flux members. A similar result is found when the same analysis is performed in the NCEP forecasts (see Figure S2).

Next we compare the evolution of the S-G dipole with that of the Ural high (after Karpechko et al. (2018)) (Figure 5). The S-G dipole peaked at 52 hPa in ERA-Interim on 5 February. There is rapid divergence after 3 February in accordance with Figure 4 (due to discrepancies in both nodes of the dipole), whilst it is also shown that the ensemble members with the largest heat flux more closely follow ERA-Interim verification. There is also a lagged relationship between the S-G dipole evolution and the Ural high, and ensemble members with lowest mean 300 hPa heat flux lack both a strong S-G dipole and Ural high. Inspecting potential vorticity (PV) on the 320 K isentropic surface in ensemble members with the top 10% mean 300 hPa heat flux (Figure 6a) shows a tongue of low PV air (<2 PVU) protruding polewards in the Atlantic sector east of Greenland on 5 February before becoming cut-off and overturning on 8 February, indicative of an anticyclonic Rossby wave break. This evolution is spatially and temporally coherent with both the cyclone track/S-G dipole development and the 300 hPa heat flux. The wave break is not present in ensemble members with the lowest 10% heat flux, which correspondingly lacked a strong S-G dipole (Figure 6b). Thus, the predictability of the wave breaking event and its impact on the stationary wave pattern indicates a possible explanation for the abrupt forecast transition, as well as a dynamical mechanism by which the S-G dipole in MSLP relates to both enhanced wave activity and amplification of the Ural high downstream (through the attendant upper-level PV anomaly).

The relationship between the S-G dipole, the Ural high, and 300 hPa heat flux in February 2018 is shown in Figure 7. Forecast heat flux increases approximately linearly with S-G dipole strength ($r = 0.79$ in NCEP vs. 0.75 in ECMWF) and heat flux is only enhanced for values of the S-G dipole above ∼40 hPa. However, not all ensemble members with an enhanced dipole produce enhanced heat flux; members with the strongest heat flux feature both an amplified S-G dipole *and* a strengthened Ural high. Thus, the enhancement of wave activity and amplification of the Ural high was dependent upon the prior occurrence of the S-G dipole/wave breaking event as well as specifics of the wave break and its interaction with the stratosphere. Figure 8 illustrates the surface evolution of the Ural high over 6–8 February in high vs. low heat flux members (c.f. Figure 4 and Figure S3). The anticyclone that develops over the Urals on 8 February in the high heat flux members is the same system that is present over Scandinavia in the preceding days associated with one node of the S-G dipole; this anticyclone is absent in the low heat flux members, and thus directly links the evolution of the Ural high to the S-G dipole. Therefore, the two precursors are not independent.

3.3 Historical S-G Dipoles

In this section we consider historical cases in extended-winter (November–March) where the S-G dipole exceeds 40 hPa (similar in magnitude to the 2018 event, and approximately equal to the 99^{th} percentile of daily November–March 1979-2017 ERA-Interim climatology) to discern whether the dipole is a characteristic of previous cases of SPV weakening. This threshold is not influenced by the time of year of an individual event, as there is little day-to-day variability in the daily-mean and standard deviation of the S-G dipole through the extended winter period. The Ural high is also considered, and by using these previous examples we seek to understand whether the dipole or the Ural high was the root cause of the enhanced vertical wave activity.

Motivated by Charlton and Polvani (2007) and their consideration of stratospheric radiative timescales, we use a window of 20 days to separate individual events, yielding a total of 49 cases (listed in Table S1). The strongest S-G dipole, 56 hPa, occurred on 15 March 2015. In Figure 9 we see the MSLP lag-composite anomaly evolution, with a cyclone tracking up eastern Greenland into the Arctic region and a concomitant anticyclone over Scandinavia. Notably the anticyclone is of greater persistence throughout this period with transient amplification upon the passage of the cyclone. Following the

dipole peak, the anomaly field resembles the Scandinavian blocking Atlantic weather regime (Cassou, Terray, Hurrell, & Deser, 2004; Charlton-Perez, Ferranti, & Lee, 2018) and is similar to the precursors to weak SPV episodes shown in Kolstad and Charlton-Perez (2011).

These historical events are also associated with anticyclonic wave breaking (Figure 10) similar to that which occurred in 2018, with the wave break in the Atlantic and northern Europe evident through the reversal of the meridional PV gradient on the 315 K isentropic surface in this region. Composites of 45–75°N [v*T*] and 60–90°N geopotential height for 30 days before and after the peak of the dipole are shown in Figure 11. Strong S-G dipoles are associated with a significant vertical wave pulse, and a weakening of the SPV (increasing polar cap geopotential heights indicating a negative stratospheric NAM tendency) in 10–15 days. It should be emphasized that these results show relative vortex weakening, rather than the development of a climatologically weak vortex. Indeed, some cases show a weakening of a strong SPV, or a temporary reduction in the rate of vortex intensification, following an S-G dipole event. The evolution in 2018 (not shown) is very similar to the composites, albeit with increased magnitude.

To discern whether these historically strong S-G dipoles were also associated with enhanced Ural highs, we analyse the change in the Ural high at a 3-day lag from the dipole peak (motivated by the evolution in 2018). There is no clear tendency toward either a strengthening or a weakening Ural high ($\mu = 0.3$ hPa, $\sigma = 10.3$ hPa). Splitting the composites by whether the Ural high weakens or strengthens does not significantly alter the composites: strong S-G dipoles followed by a weakening of the Ural high still show enhanced heat flux and a weakened polar vortex in the following days. This indicates it is the wave break associated with the S-G dipole, not the resultant Ural high, which drives the enhanced vertical wave flux - and that instead, in 2018, the Ural high was a consequence of the preceding evolution.

Next, we assess the association between the S-G dipole and observed major midwinter SSWs prior to 2018 (Table 1). Of the 23 SSWs (Karpechko et al., 2017), we find 8 (35%) followed a similar evolution to 2018 and were preceded by an S-G dipole exceeding 40 hPa within 15 days of the start date of the SSW. Given the total of 345 days preceding the 23 events (and assuming independence), this is 2.3 times larger than the climatological likelihood (since 40 hPa is approximately the 99^{th} percentile, it would be

expected that it was exceeded on 3-4 days). We note that the 2018 event was stronger than any of these prior events associated with major SSWs (the previous strongest being 48 hPa preceding the major SSW in March 1981), possibly a facet of 2018 being the event used to define the index. Although the major SSW in February 2018 was a vortex split, 6 of the observed SSWs with a strong S-G dipole precursor were displacement events (Karpechko et al., 2017) suggesting this pattern does not itself induce a specific stratospheric evolution but acts to amplify an existing planetary wave structure. When 2018 is included, 78% of the major SSWs preceded by an amplified S-G dipole were downward-propagating (Karpechko et al., 2017), with only March 1981 and February 2008 otherwise. This is larger than the observed ratio of 57% (although the sample is too small to draw robust conclusions), but is in agreement with Birner and Albers (2017) who note larger tropospheric impacts following SSWs preceded by enhanced tropospheric wave activity. We further note that 33% (90%) of the S-G dipole events considered here were associated with daily 500 hPa [v*T*] exceeding 2 σ (1 σ) within 5 days either side of the events, indicating the dipole is an important contributor to anomalously high zonal-mean tropospheric wave flux in general.

4 Discussion and Conclusions

In this study we have shown that the abrupt onset of predictions of stratospheric polar vortex (SPV) weakening and sudden stratospheric warming (SSW) in February 2018 was driven by an anticyclonic Rossby wave break (Figure 6) associated with the track and intensity of a cyclone over eastern Greenland, and an associated ridge over Scandinavia. From this, we define a Scandinavia-Greenland (S-G) dipole index in MSLP to describe the evolution, and show that this was not well-forecast at long lead-times. The location and intensity of the cyclone was a rare occurrence, with the mean MSLP in the Greenland node and the dipole itself exceeding the 99th percentile of extended winter months from 1979-2017. Occurrences of similarly strong S-G dipoles in reanalysis are shown to be associated with anticyclonic wave breaking in the Atlantic sector (Figure 10), which induces anomalously strong vertical wave activity (Figure 11a), and a rapid tendency towards a weakened SPV/negative stratospheric NAM (Figure 11b) within 10 days. This indicates that the evolution in 2018 was not a characteristic of the specific flow configuration but a more general mechanism for vortex weakening present in other events.

We have also shown that the S-G dipole and wave breaking event was important for amplifying a high pressure system over the Urals, first described in Karpechko et al. (2018) as a surface-pressure precursor of the 2018 SSW. Our results suggest that the Ural high was likely a consequence of the wave breaking event which drove stratospheric wave activity leading to the SSW, rather than a primary driver itself. The initial divergence in the evolution of the SPV strength and the onset of the enhanced vertical wave flux occurred around 5 February (Figure 2), preceding the amplification of the Ural high which followed on 8 February (Figure 5b), which further indicates the Ural high was a secondary response. It is likely that the persistence of the Ural high might have resulted in its detection in the averaging used in Karpechko et al. (2018), rather than the transience of the S-G dipole/wave break.

Our results differ from previous work through using a 'bottom-up' perspective, assessing the stratospheric response to tropospheric events. We provide a particular *transient* trigger which would not be easily distinguished through 'top-down' time-mean composites (where the tropospheric configuration prior to stratospheric events is considered). This helps illuminate mechanisms by which persistent tropospheric blocking, including Scandinavian blocking which has previously been shown to precede SSWs (Cohen & Jones, 2011; Kolstad & Charlton-Perez, 2011; Martius et al., 2009), can produce *sudden* changes in the stratospheric circulation. Furthermore, our results apply to a wider range of SPV variability than major SSWs – even the case of weakening a climatologically strong vortex towards an average state – which helps describe precursors of a larger proportion of the sub-seasonal behaviour. We therefore suggest the S-G dipole should be monitored operationally as a precursor to SPV weakening. Changes and uncertainty in its forecasts may help to qualitatively identify sources of uncertainty in stratospheric forecasts.

The intensity of the S-G dipole in 2018 was not well-forecast, driven by uncertainty in the track and intensity of an Atlantic cyclone. At longer lead-times, model biases in storm track and intensity may negatively impact the skill in predicting such events. For example, Frame, Methven, Roberts, and Titley (2015) showed cyclone intensity decayed with lead-time up to 15 days, which would constrain the ability of forecast models to produce strong S-G dipoles sufficient for strong wave breaking and vortex weakening, whilst Gray, Dunning, Methven, Masato, and Chagnon (2014) and Saffin, Gray, Methven, and Williams (2017) also showed biases in tropopause PV and Rossby wave structure which may limit the ability to capture these types of wave breaking episodes and associated

stratospheric variability. These considerations are consistent with a deterministic limit on SSW predictability (Karpechko, 2018; Taguchi, 2018).

The occurrence of strong S-G dipoles requires a poleward-shifted Atlantic storm track, which is associated with the positive NAM/NAO pattern. This is often related to the prior occurrence of a strengthened SPV (e.g. Baldwin & Dunkerton, 2001) and SSWs are typically preceded by strong SPV conditions (e.g. Charlton & Polvani, 2007). This behaviour could imply a two-way coupling in which the vortex drives its own variability - akin to a self-sustaining oscillator. Several studies (e.g. Lorenz & DeWeaver, 2007; Tamarin & Kaspi, 2017) have indicated a poleward shift in the North Atlantic storm track during winter under future climate change. This may lead to an increased frequency of strong S-G dipoles and thus more frequent wave breaking events and stratospheric vortex weakening, but the aforementioned biases may reduce the ability of climate models to fully represent this source of sub-seasonal variability.

Acknowledgments

S.H.L. was funded by the Natural Environment Research Council (NERC) via the SCENARIO Doctoral Training Partnership (NE/L002566/1) at the University of Reading. S.J.W. was supported by the National Centre for Atmospheric Science, a NERC collaborative centre, under contract R8/H12/83/001. This work is based on S2S data, a joint initiative of the World Weather Research Programme (WWRP) and the World Climate Research Programme (WCRP). S2S and ERA-Interim reanalysis data are available online at https://apps.ecmwf.int/datasets/. Pre-processing of data used here was completed as part of the WCRP SPARC SNAP (Stratosphere-troposphere Processes and their Role in Climate: Stratospheric Network for the Assessment of Predictability) programme. The authors acknowledge three anonymous reviewers for their helpful suggestions.

References

Andrews, D., Holton, J., & Leovy, C. (1987). *Middle Atmosphere Dynamics*. Academic Press.

Attard, H. E., & Lang, A. L. (2019). Troposphere-stratosphere coupling following tropospheric blocking and extratropical cyclones. *Monthly Weather Review*, MWR–D–18–0335.1. doi: 10.1175/MWR-D-18-0335.1

Baldwin, M. P., & Dunkerton, T. J. (2001). Stratospheric harbingers of anomalous

weather regimes. *Science*, *294*(5542), 581–584. doi: 10.1126/science.1063315

Bao, M., Tan, X., Hartmann, D. L., & Ceppi, P. (2017). Classifying the tropospheric precursor patterns of sudden stratospheric warmings. *Geophysical Research Letters*, *44*(15), 8011–8016. doi: 10.1002/2017GL074611

Birner, T., & Albers, J. R. (2017). Sudden stratospheric warmings and anomalous upward wave activity flux. *Sola*, *13A*(Special_Edition), 8–12. doi: 10.2151/sola.13a-002

Butler, A. H., Sjoberg, J. P., Seidel, D. J., & Rosenlof, K. H. (2017). A sudden stratospheric warming compendium. *Earth System Science Data*, *9*(1), 63–76. doi: 10.5194/essd-9-63-2017

Cassou, C., Terray, L., Hurrell, J. W., & Deser, C. (2004). North Atlantic winter climate regimes: spatial asymmetry, stationarity with time, and oceanic forcing. *Journal of Climate*, *17*(5), 1055–1068. doi: 10.1175/1520-0442(2004)017⟨1055:NAWCRS⟩2.0.CO;2

Charlton, A. J., & Polvani, L. M. (2007). A new look at stratospheric sudden warmings. part i: climatology and modelling benchmarks. *J. Climate*, *20*(3), 449-469. doi: 10.1175/JCLI3996.1

Charlton-Perez, A. J., Ferranti, L., & Lee, R. W. (2018). The influence of the stratospheric state on North Atlantic weather regimes. *Quarterly Journal of the Royal Meteorological Society*, *144*(713), 1140–1151. doi: 10.1002/qj.3280

Cohen, J., & Jones, J. (2011). Tropospheric precursors and stratospheric warmings. *Journal of Climate*, *25*(5), 1780–1790. doi: 10.1175/JCLI-D-11-00701.1

Colucci, S. J., & Kelleher, M. E. (2015). Diagnostic comparison of tropospheric blocking events with and without sudden stratospheric warming. *Journal of the Atmospheric Sciences*, *72*(6), 2227–2240. doi: 10.1175/jas-d-14-0160.1

Coy, L., Eckermann, S., & Hoppel, K. (2009). Planetary wave breaking and tropospheric forcing as seen in the stratospheric sudden warming of 2006. *Journal of the Atmospheric Sciences*, *66*(2), 495–507. doi: 10.1175/2008jas2784.1

Coy, L., & Pawson, S. (2014). The major stratospheric sudden warming of January 2013: analyses and forecasts in the GEOS-5 data assimilation system. *Monthly Weather Review*, *143*(2), 491–510. doi: 10.1175/mwr-d-14-00023.1

Dee, D. P., Uppala, S. M., Simmons, A. J., Berrisford, P., Poli, P., Kobayashi, S., ... Vitart, F. (2011). The ERA-Interim reanalysis: configuration and performance

of the data assimilation system. *Quarterly Journal of the Royal Meteorological Society*, *137*(656), 553–597. doi: 10.1002/qj.828

Ferranti, L., Magnusson, L., Vitart, F., & Richardson, D. (2018). A new product to flag up the risk of cold spells in Europe weeks ahead. *ECMWF Newsletter*(158), 1–8. doi: 10.21957/k2rlf88oe1

Frame, T. H. A., Methven, J., Roberts, N. M., & Titley, H. A. (2015). Predictability of frontal waves and cyclones. *Weather and Forecasting*, *30*(5), 1291–1302. doi: 10.1175/waf-d-15-0039.1

Garfinkel, C. I., Hartmann, D. L., & Sassi, F. (2010). Tropospheric precursors of anomalous northern hemisphere stratospheric polar vortices. *Journal of Climate*, *23*(12), 3282–3299. doi: 10.1175/2010JCLI3010.1

Gray, S. L., Dunning, C. M., Methven, J., Masato, G., & Chagnon, J. M. (2014). Systematic model forecast error in Rossby wave structure. *Geophysical Research Letters*, *41*(8), 2979–2987. doi: 10.1002/2014GL059282

Julian, P. R., & Labitzke, K. B. (1965). A study of atmospheric energetics during the January–February 1963 stratospheric warming. *Journal of the Atmospheric Sciences*, *22*(6), 597–610. doi: 10.1175/1520-0469(1965)022⟨0597:asoaed⟩2.0.co;2

Karpechko, A. Y. (2018). Predictability of sudden stratospheric warmings in the ECMWF extended-range forecast system. *Monthly Weather Review*, *146*(4), 1063–1075. doi: 10.1175/MWR-D-17-0317.1

Karpechko, A. Y., Charlton-Perez, A., Balmaseda, T. N., Magdalena, & Vitart, F. (2018). Predicting sudden stratospheric warming 2018 and its climate impacts with a multimodel ensemble. *Geophysical Research Letters*, *45*(24), 13,538–13,546. doi: 10.1029/2018GL081091

Karpechko, A. Y., Hitchcock, P., Peters, D. H. W., & Schneidereit, A. (2017). Predictability of downward propagation of major sudden stratospheric warmings. *Quarterly Journal of the Royal Meteorological Society*, *143*(704), 1459–1470. doi: 10.1002/qj.3017

Kolstad, E. W., & Charlton-Perez, A. J. (2011). Observed and simulated precursors of stratospheric polar vortex anomalies in the Northern Hemisphere. *Climate Dynamics*, *37*(7-8), 1443–1456. doi: 10.1007/s00382-010-0919-7

Krüger, K., Naujokat, B., & Labitzke, K. (2005). The unusual midwinter warming in

the Southern Hemisphere stratosphere 2002: a comparison to Northern Hemisphere phenomena. *Journal of the Atmospheric Sciences*, *62*(3), 603–613. doi: 10.1175/jas-3316.1

Lorenz, D. J., & DeWeaver, E. T. (2007). Tropopause height and zonal wind response to global warming in the IPCC scenario integrations. *Journal of Geophysical Research Atmospheres*, *112*(10), 1–11. doi: 10.1029/2006JD008087

Martius, O., Polvani, L. M., & Davies, H. C. (2009). Blocking precursors to stratospheric sudden warming events. *Geophysical Research Letters*, *36*(14), 1–5. doi: 10.1029/2009GL038776

O'Neill, A., Oatley, C. L., Charlton-Perez, A. J., Mitchell, D. M., & Jung, T. (2017). Vortex splitting on a planetary scale in the stratosphere by cyclogenesis on a subplanetary scale in the troposphere. *Quarterly Journal of the Royal Meteorological Society*, *143*(703), 691–705. doi: 10.1002/qj.2957

Peings, Y. (2019). Ural blocking as a driver of early winter stratospheric warmings. *Geophysical Research Letters*, 2019GL082097. doi: 10.1029/2019GL082097

Quiroz, R. S. (1986). The association of stratospheric warmings with tropospheric blocking. *Journal of Geophysical Research*, *91*(D4), 5277. doi: 10.1029/jd091id04p05277

Saffin, L., Gray, S. L., Methven, J., & Williams, K. D. (2017). Processes maintaining tropopause sharpness in numerical models. *Journal of Geophysical Research: Atmospheres*, *122*(18), 9611–9627. doi: 10.1002/2017JD026879

Taguchi, M. (2014). Predictability of major stratospheric sudden warmings of the vortex split type: case study of the 2002 southern event and the 2009 and 1989 northern events. *Journal of the Atmospheric Sciences*, *71*(8), 2886–2904. doi: 10.1175/jas-d-13-078.1

Taguchi, M. (2018). Comparison of subseasonal-to-seasonal model forecasts for major stratospheric sudden warmings. *Journal of Geophysical Research: Atmospheres*, *123*(18), 10,231–10,247. doi: 10.1029/2018JD028755

Tamarin, T., & Kaspi, Y. (2017). The poleward shift of storm tracks under global warming: a Lagrangian perspective. *Geophysical Research Letters*, *44*(20), 10,666–10,674. doi: 10.1002/2017GL073633

Thompson, D. W., & Wallace, J. M. (2000). Annular modes in the extratropical circulation. Part I: month-to-month variability. *Journal of Climate*, *13*(5), 1000–

1016. doi: 10.1175/1520-0442(2000)013⟨1000:AMITEC⟩2.0.CO;2

Tripathi, O. P., Baldwin, M., Charlton-Perez, A., Charron, M., Cheung, J. C. H., Eckermann, S. D., ... Stockdale, T. (2016). Examining the predictability of the stratospheric sudden warming of January 2013 using multiple NWP systems. *Monthly Weather Review*, *144*(5), 1935–1960. doi: 10.1175/MWR-D-15-0010.1

Tripathi, O. P., Baldwin, M., Charlton-Perez, A., Charron, M., Eckermann, S. D., Gerber, E., ... Son, S. W. (2015). The predictability of the extratropical stratosphere on monthly time-scales and its impact on the skill of tropospheric forecasts. *Quarterly Journal of the Royal Meteorological Society*, *141*(689), 987–1003. doi: 10.1002/qj.2432

Vitart, F., Ardilouze, C., Bonet, A., Brookshaw, A., Chen, M., Codorean, C., ... Zhang, L. (2017). The subseasonal to seasonal (S2S) prediction project database. *Bulletin of the American Meteorological Society*, *98*(1), 163–173. doi: 10.1175/BAMS-D-16-0017.1

White, I., Garfinkel, C. I., Gerber, E. P., Jucker, M., Aquila, V., & Oman, L. D. (2019). The downward influence of sudden stratospheric warmings: association with tropospheric precursors. *Journal of Climate*, *32*(1), 85–108. doi: 10.1175/JCLI-D-18-0053.1

514 **Table 1.** Major SSWs in the period 1979–2017 (following Karpechko et al. (2017)) and the
515 peak value of the S-G dipole in the 15 days before the event according to ERA-Interim reanaly-
516 sis. Those events exceeding 40 hPa are shown in bold.

SSW event	Peak S-G index (hPa)
February 1979	**41**
February 1980	**43**
March 1981	**48**
December 1981	13
February 1984	**45**
January 1985	**44**
January 1987	**43**
December 1987	26
March 1988	21
February 1989	39
December 1998	34
February 1999	18
March 2000	24
February 2001	31
December 2001	24
January 2003	2
January 2004	12
January 2006	**42**
February 2007	17
February 2008	**40**
January 2009	22
February 2010	36
January 2013	27

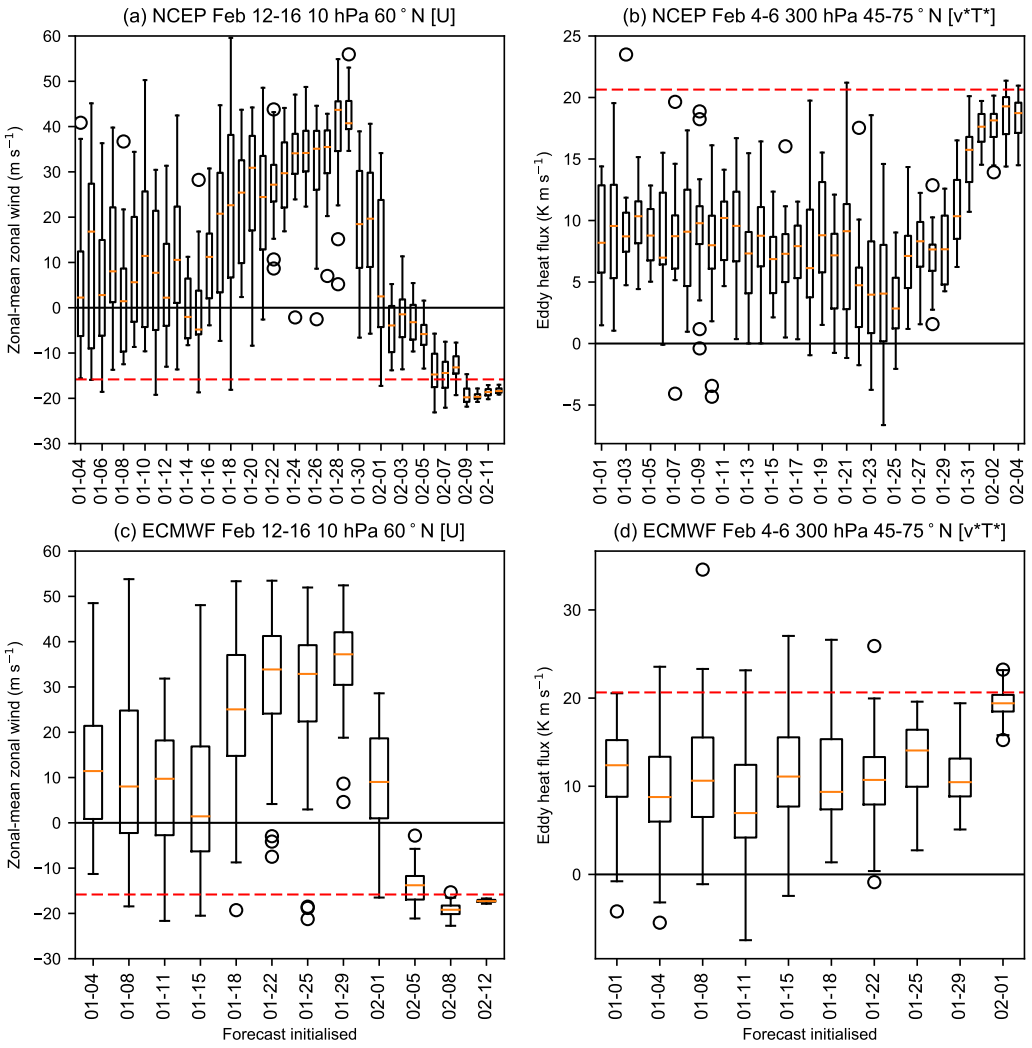

Figure 1. Boxplots showing (a), (c) average 10 hPa 60°N zonal-mean zonal-winds for 12–16 February 2018 and (b), (d) 300 hPa 45–75°N meridional eddy heat flux averaged over 4–6 February 2018 in (a), (b) NCEP and (c), (d) ECMWF models for all ensemble members as a function of initialisation date. Boxes indicate the interquartile range (IQR), whiskers extend to the last point less or greater than 1.5 times the IQR, with circles indicating outliers. The dashed red lines indicate verifying values according to ERA-Interim reanalysis.

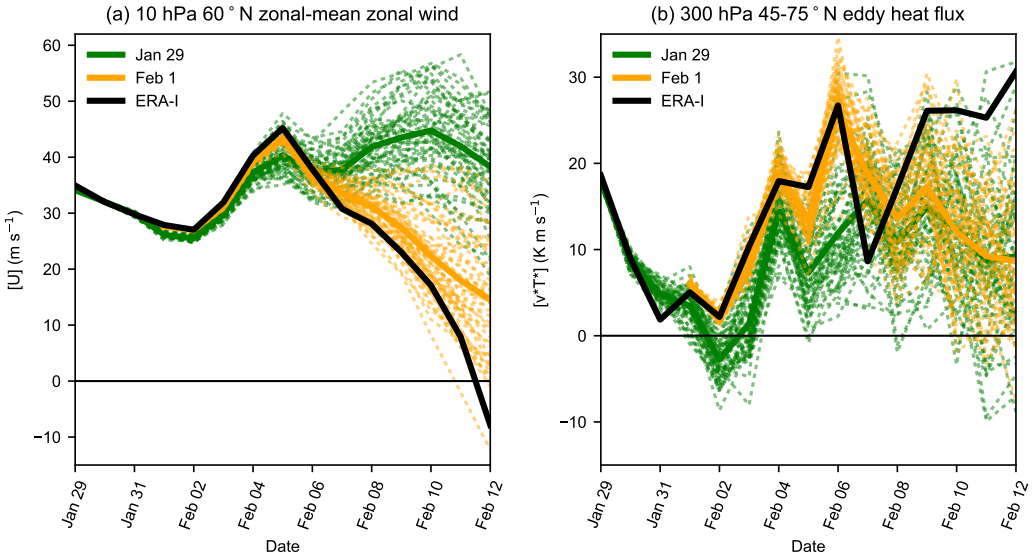

Figure 2. ECMWF ensemble forecasts from 29 January (dashed green) and 1 February (dashed orange) for (a) 10 hPa 60°N zonal-mean zonal wind and (b) 300 hPa 45–75°N meridional eddy heat flux for 29 January–12 February 2018. Ensemble means are shown with thick lines. Verifying evolution from ERA-Interim is shown with the thick black line.

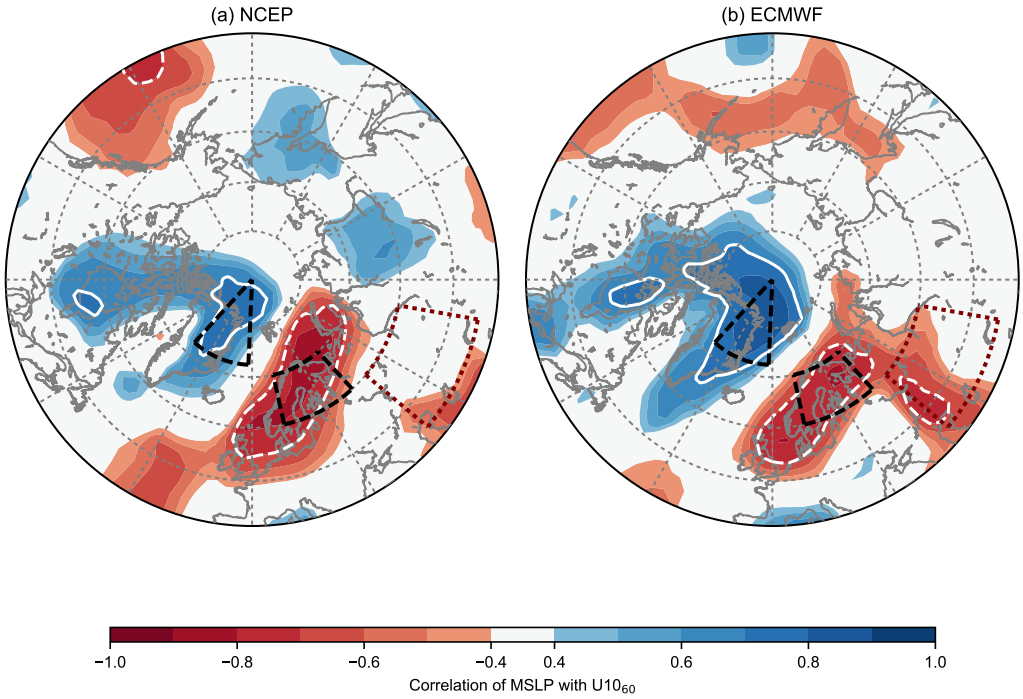

Figure 3. Linear correlation between average 9–11 February $U10_{60}$ and average 3–5 February mean MSLP from (a) 29 January to 1 February NCEP forecasts and (b) 29 January and 1 February ECMWF forecasts. White lines delineate where the magnitude of the correlation exceeds 0.7. The two nodes of the S-G dipole are shown with black dashed lines, and the location of the Ural high is shown with maroon dotted lines.

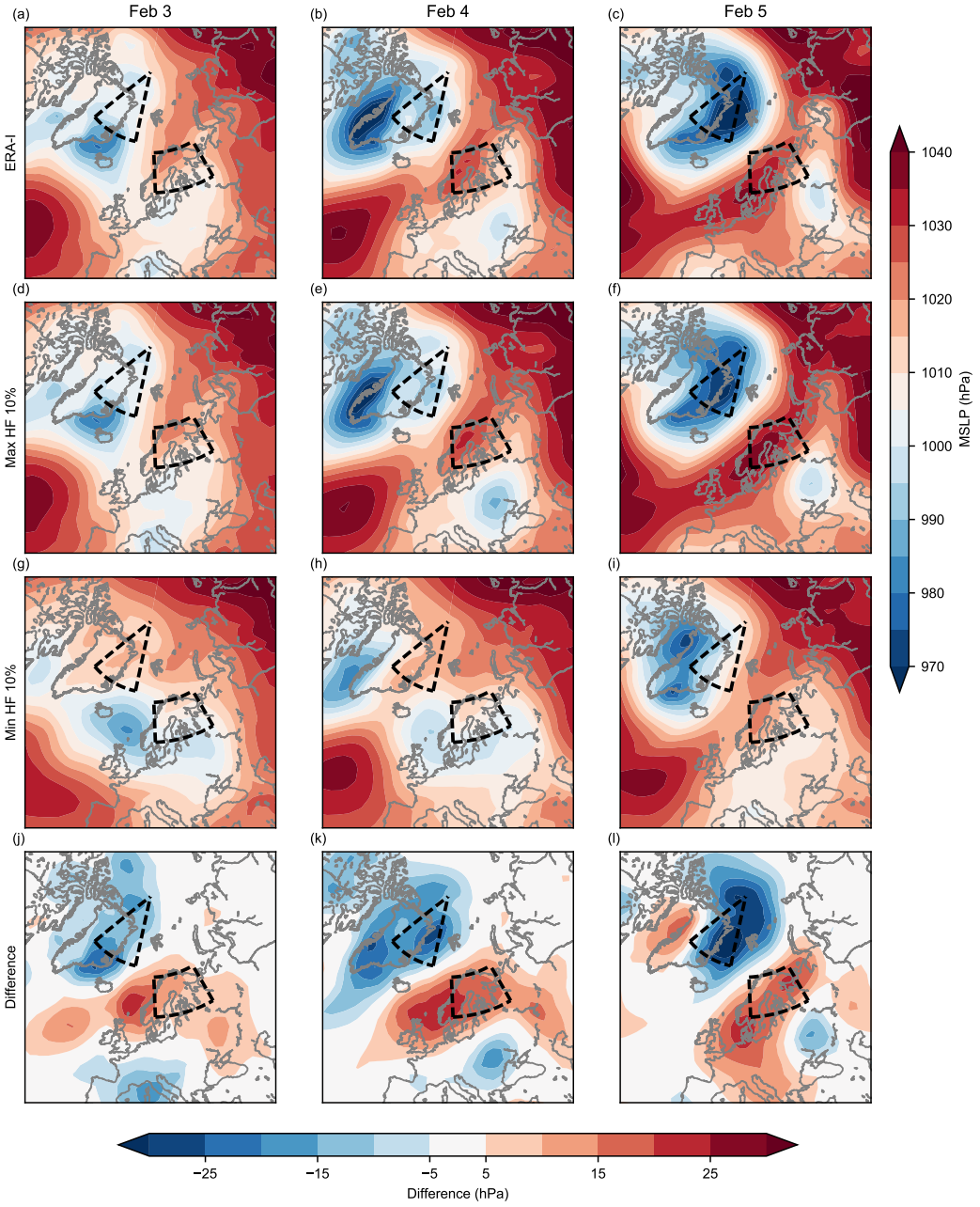

532 **Figure 4.** MSLP for 3–5 February from (a-c) ERA-Interim reanalysis, (d-f) the mean forecast
533 from members of the ECMWF 29 January and 1 February joined ensemble with the top 10% 300
534 hPa 45–75°N heat flux on 4–6 February, (g-i) the bottom 10%, and (j-l) the difference (d-f – g-i).
535 The two nodes of the S-G dipole are shown with black dashed lines.

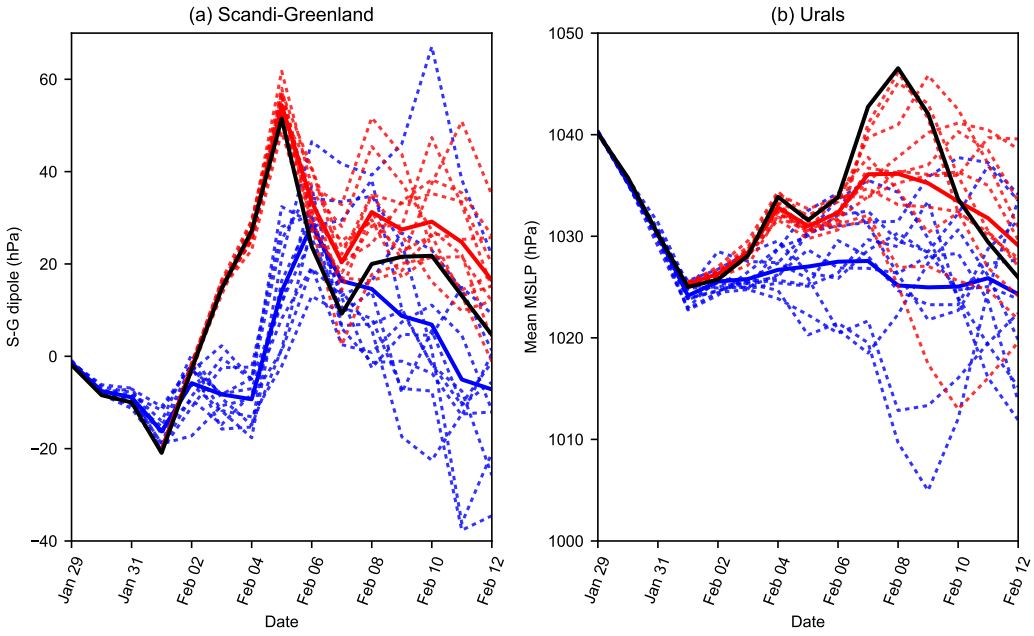

Figure 5. Time series of ECMWF ensemble forecasts from 29 January 1 February for (a) the S-G dipole and (b) the Ural high from members with the top (dotted red) and bottom (dotted blue) 10% mean 4–6 February 300 hPa 45–75°N [v*T*]. Their respective means are shown with thick lines coloured accordingly. The verifying evolution from ERA-Interim is shown in black.

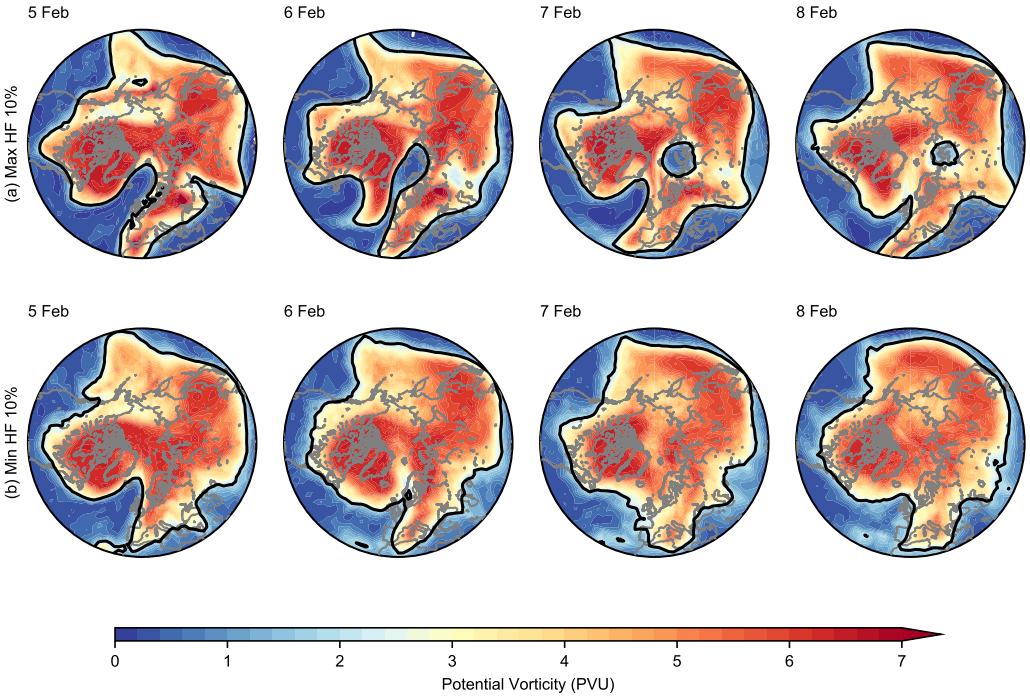

Figure 6. Forecasts of PV on the 320 K isentropic surface for 5–8 February from members of the ECMWF 29 January and 1 February joined ensemble. (a) shows the mean forecast from members with the top 10% 300 hPa 45–75°N heat flux on 4–6 February and (b) the bottom 10%. The 2 PV unit isoline (PVU, where 1 PVU = 10^{-6} m^2 s^{-1} K kg^{-1}) is contoured in black.

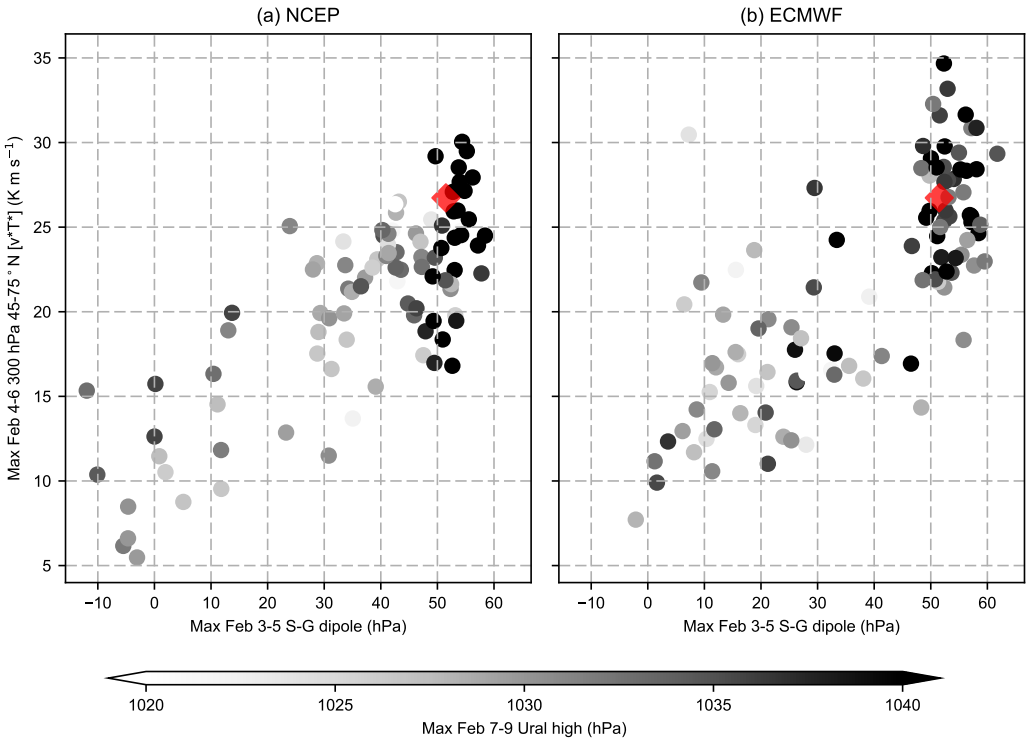

544 **Figure 7.** Scatter plots of maximum 4–6 February 300 hPa [v*T*] versus maximum 3–5
545 February mean S-G dipole for (a) NCEP ensembles from 29 January to 3 February ($n = 96$), and
546 (b) ECMWF ensembles from 29 January and 1 February ($n = 102$). The points are coloured by
547 the corresponding maximum 7–9 February Ural high strength. The verifying ERA-Interim value
548 is shown with a red diamond.

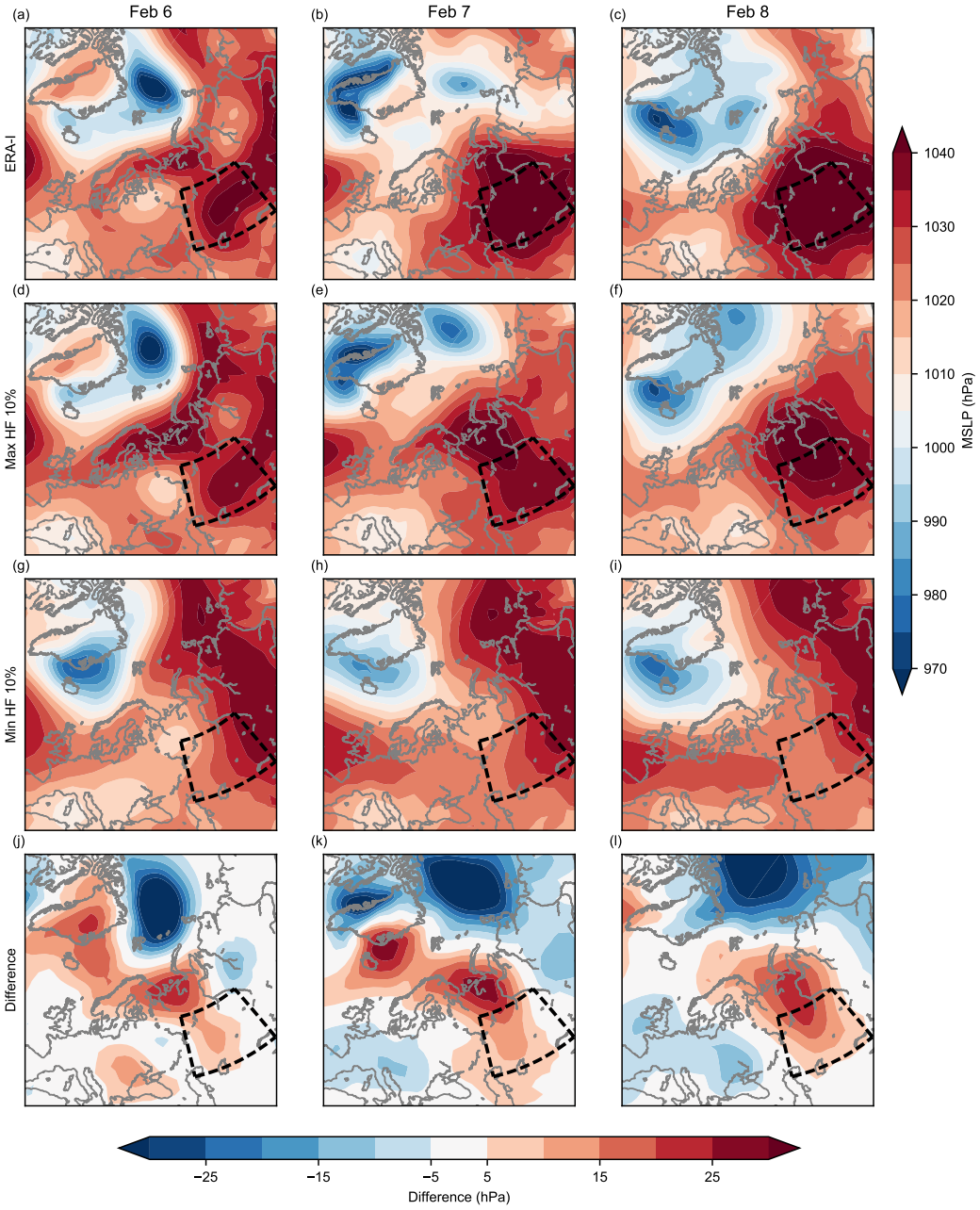

549 **Figure 8.** As in Figure 4 but for 6–8 February. The Ural high is indicated with black dashed
550 lines.

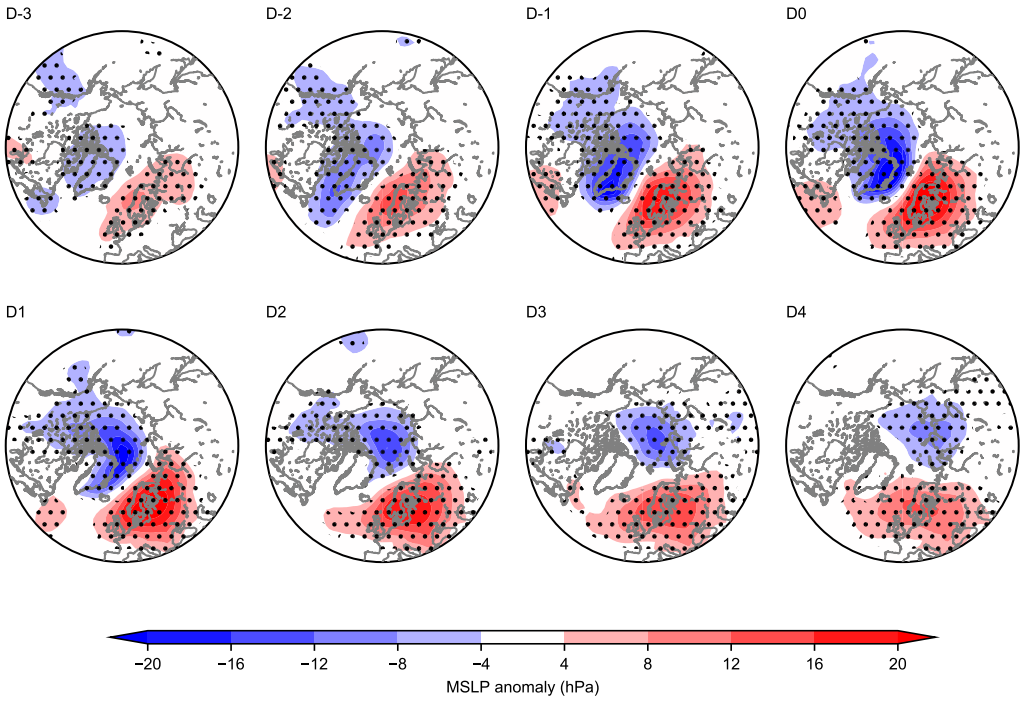

Figure 9. Composite of MSLP anomalies (with respect to January 1979–March 2017 climatology) from ERA-Interim for the period 3 days before to 4 days after 49 historical S-G dipole events exceeding 40 hPa. Stippling indicates areas significant at the 95% confidence level (for details see Section 2).

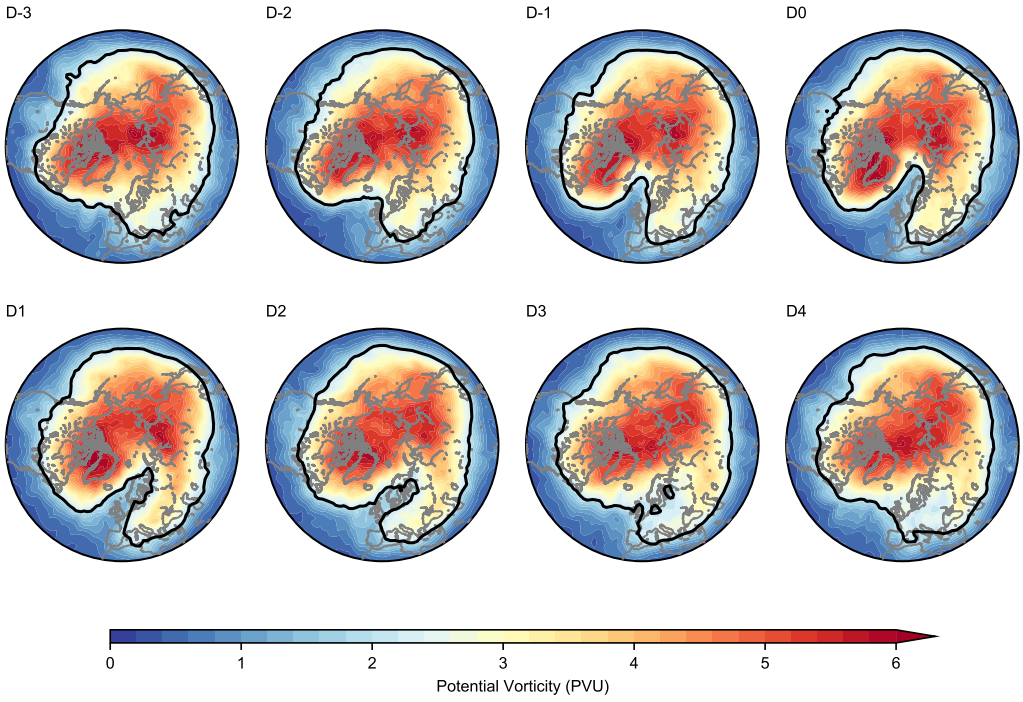

555 **Figure 10.** As in Figure 9 but for PV on the 315 K isentropic surface. The thick black line
556 indicates the 2 PVU contour.

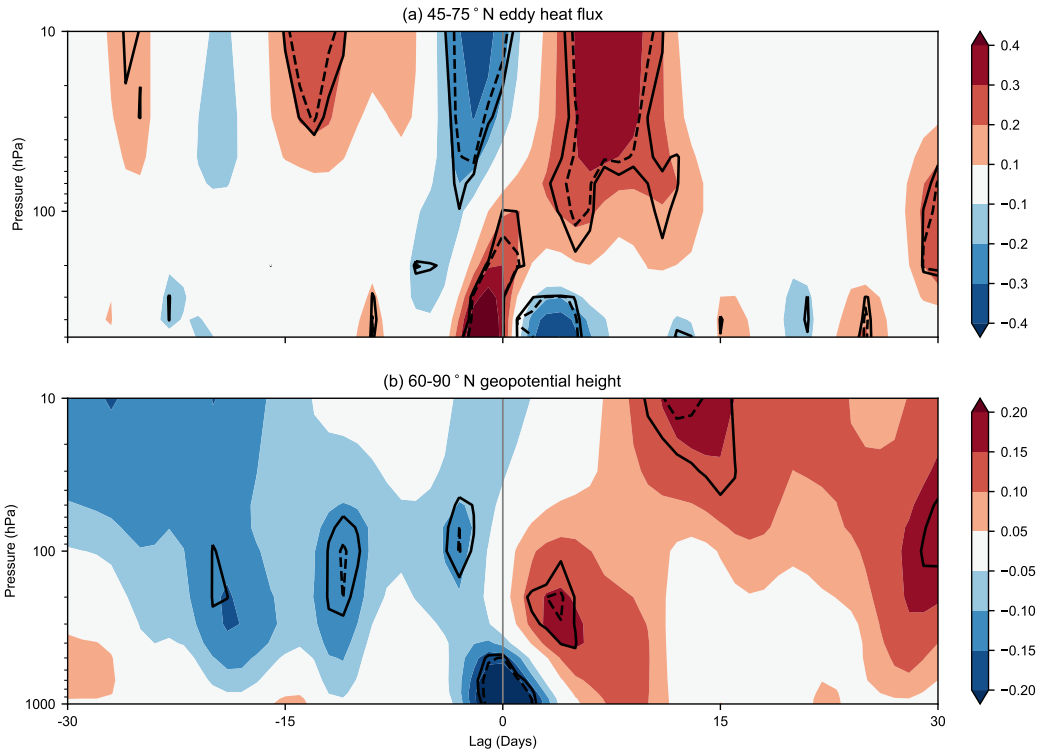

Figure 11. Composite of anomalies in (a) 45–75°N meridional eddy heat flux [v*T*] and (b) 60–90°N geopotential height for 30 days before and after 49 events in ERA-Interim 1979–2017 where the S-G dipole exceeded 40 hPa. Anomalies are standardized departures and are filtered using a 1 σ Gaussian smoother; in (b) these are shown relative to the mean for the 61-day window to show relative tendency. The gray vertical line indicates the day on which the 40 hPa threshold was exceeded. Solid (dashed) black contours indicate regions significant at the 90% (95%) confidence level (for details see Section 2).

Figure 1.

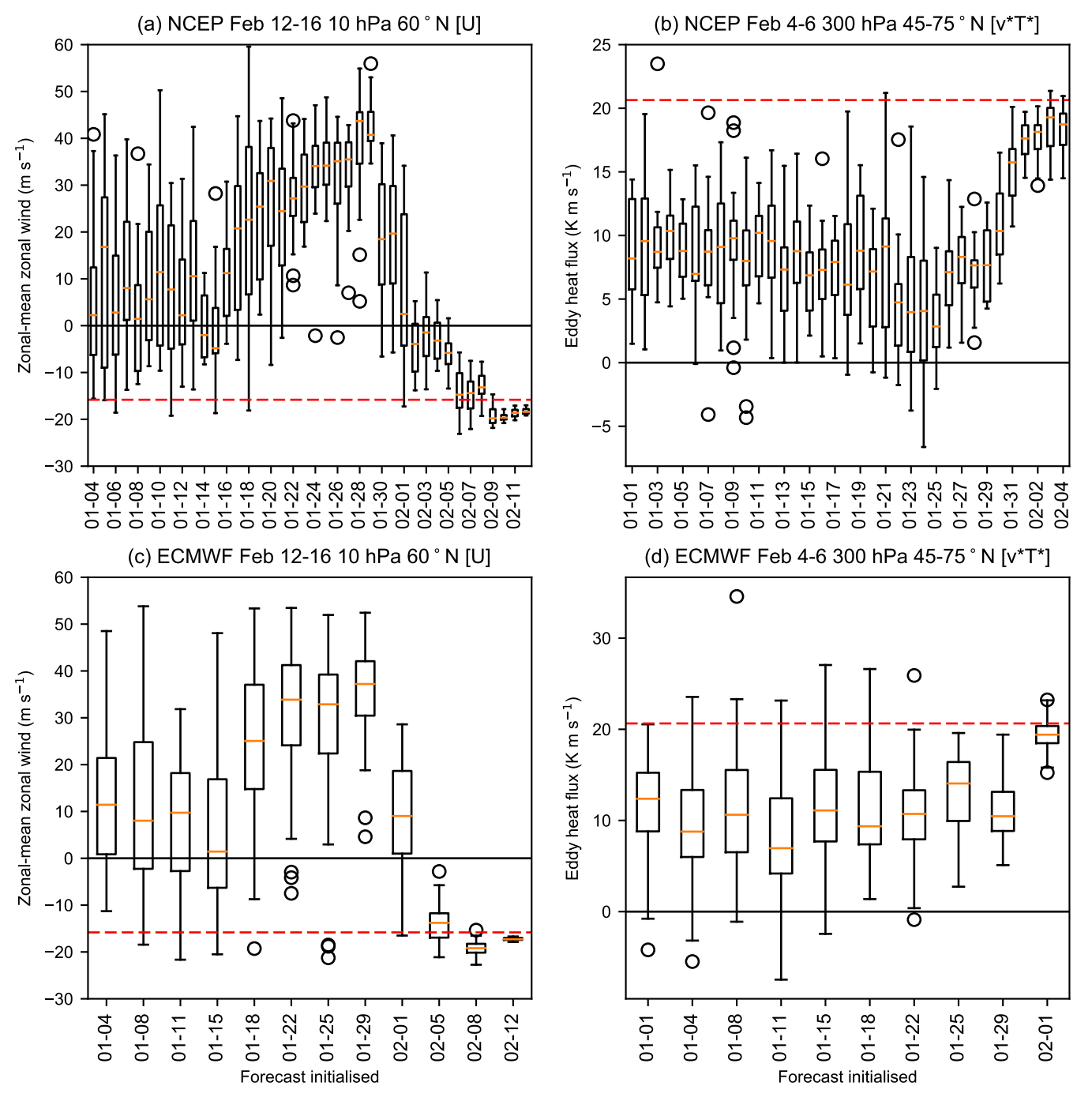
(a) NCEP Feb 12-16 10 hPa 60 ° N [U]
Zonal-mean zonal wind (m s^{-1})
60
50
40
30
20
10
0
−10
−20
−30
01-04
01-06
01-08
01-10
01-12
01-14
01-16
01-18
01-20
01-22
01-24
01-26
01-28
01-30
02-01
02-03
02-05
02-07
02-09
02-11
(b) NCEP Feb 4-6 300 hPa 45-75 ° N [v*T*]
Eddy heat flux (K m s^{-1})
25
20
15
10
5
0
−5
01-01
01-03
01-05
01-07
01-09
01-11
01-13
01-15
01-17
01-19
01-21
01-23
01-25
01-27
01-29
01-31
02-02
02-04
(c) ECMWF Feb 12-16 10 hPa 60 ° N [U]
Zonal-mean zonal wind (m s^{-1})
60
50
40
30
20
10
0
−10
−20
−30
01-04
01-08
01-11
01-15
01-18
01-22
01-25
01-29
02-01
02-05
02-08
02-12
Forecast initialised
(d) ECMWF Feb 4-6 300 hPa 45-75 ° N [v*T*]
Eddy heat flux (K m s^{-1})
30
20
10
0
01-01
01-04
01-08
01-11
01-15
01-18
01-22
01-25
01-29
02-01
Forecast initialised

Figure 2.

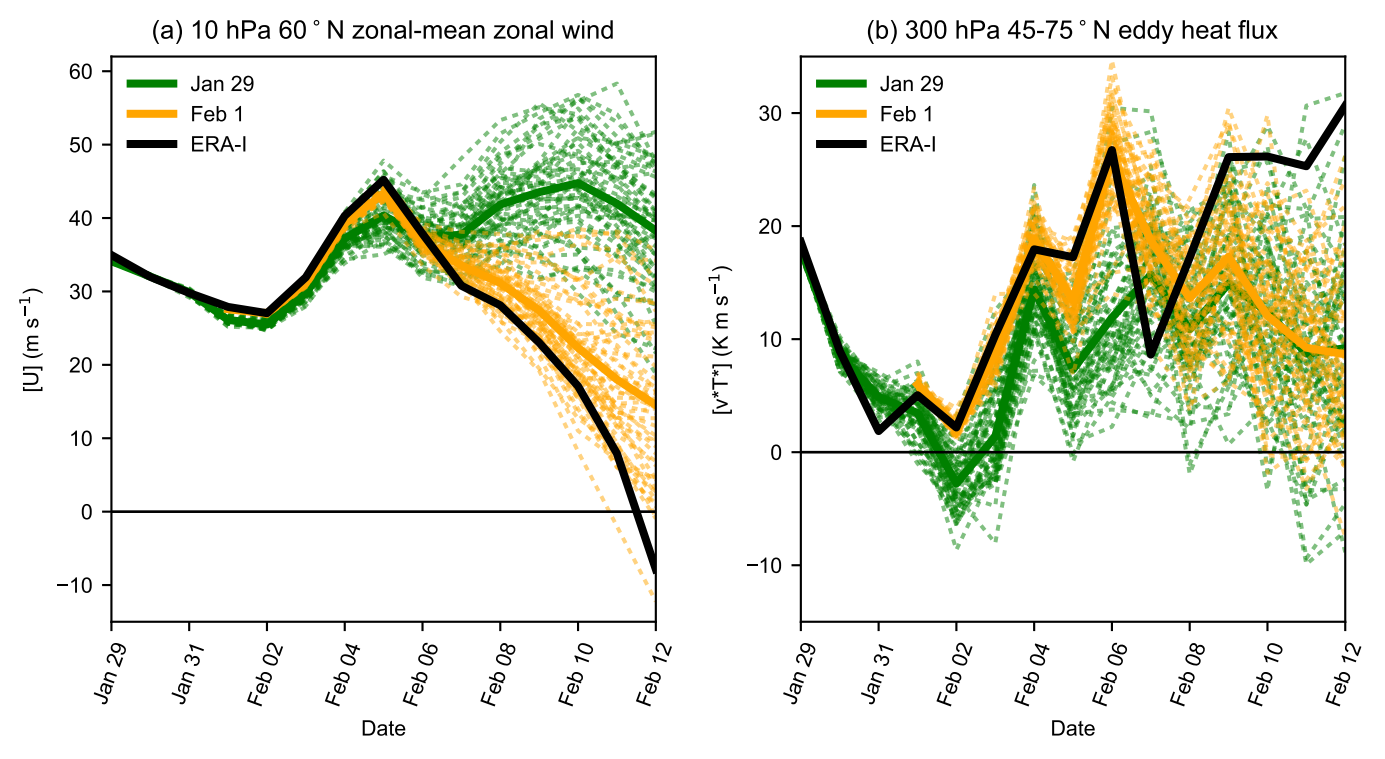
(a) 10 hPa 60 ° N zonal-mean zonal wind
Jan 29
Feb 1
ERA-I
[U] (m s^{-1})
60
50
40
30
20
10
0
−10
Jan 29
Jan 31
Feb 02
Feb 04
Feb 06
Feb 08
Feb 10
Feb 12
Date
(b) 300 hPa 45-75 ° N eddy heat flux
Jan 29
Feb 1
ERA-I
[v*T*] (K m s^{-1})
30
20
10
0
−10
Jan 29
Jan 31
Feb 02
Feb 04
Feb 06
Feb 08
Feb 10
Feb 12
Date

Figure 3.

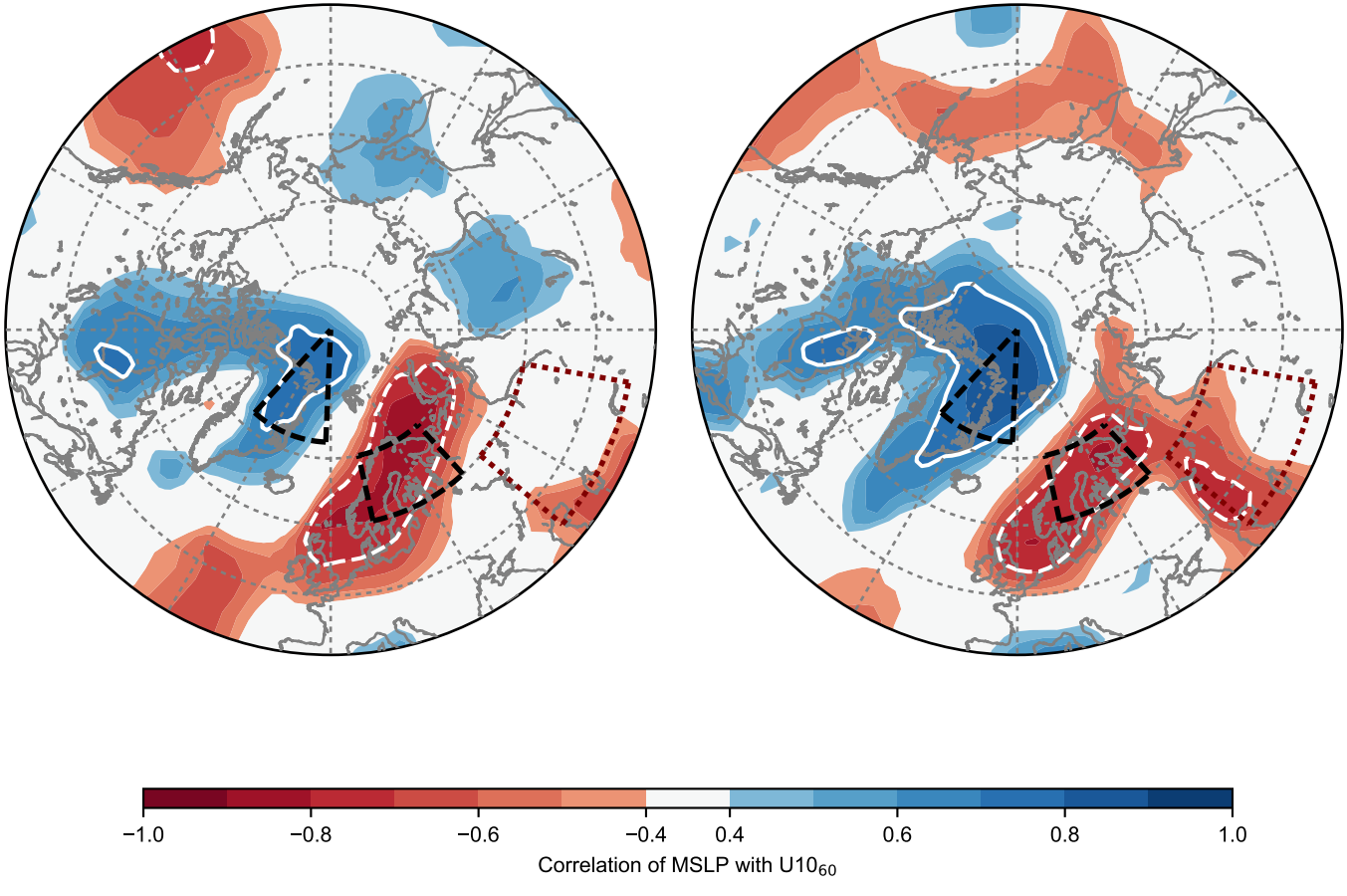
(a) NCEP
(b) ECMWF
−1.0
−0.8
−0.6
−0.4
0.4
0.6
0.8
1.0
Correlation of MSLP with U10$_{60}$

Figure 4.

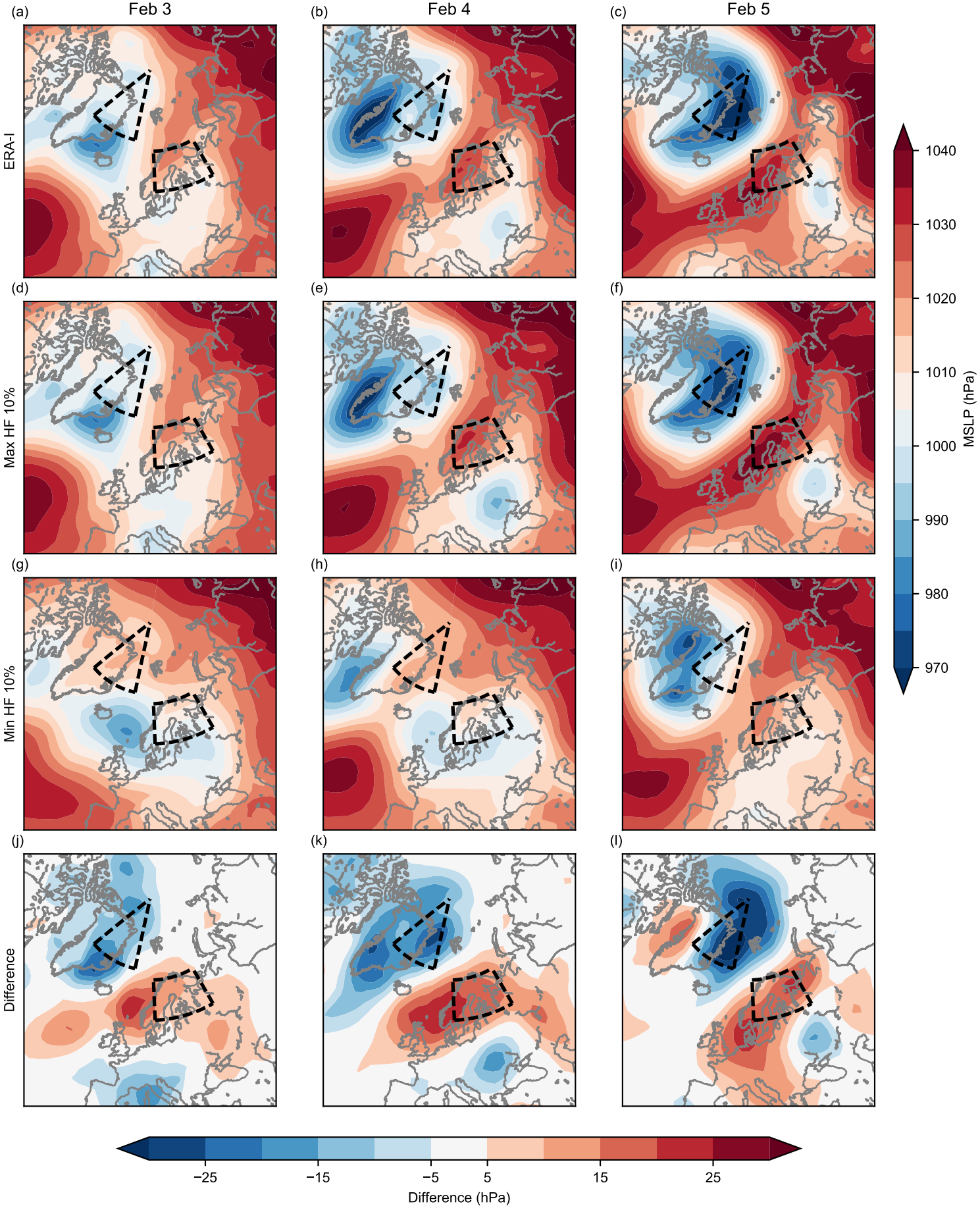
(a)
Feb 3
(b)
Feb 4
(c)
Feb 5
ERA-I
(d)
(e)
(f)
Max HF 10%
(g)
(h)
(i)
Min HF 10%
(j)
(k)
(l)
Difference
1040
1030
1020
1010
1000
990
980
970
MSLP (hPa)
−25
−15
−5
5
15
25
Difference (hPa)

Figure 5.

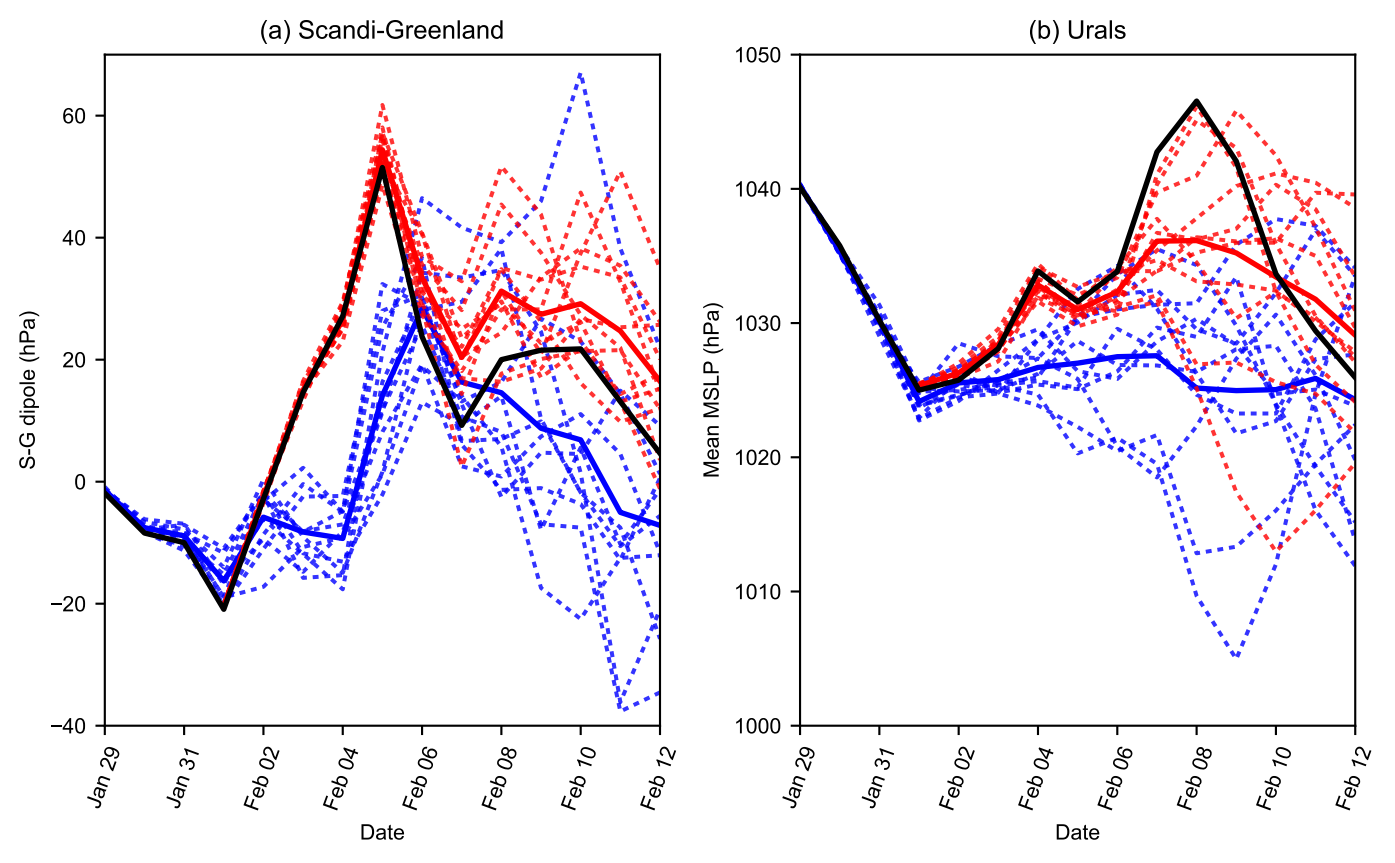
(a) Scandi-Greenland
S-G dipole (hPa)
60
40
20
0
−20
−40
Jan 29
Jan 31
Feb 02
Feb 04
Feb 06
Feb 08
Feb 10
Feb 12
Date
(b) Urals
Mean MSLP (hPa)
1050
1040
1030
1020
1010
1000
Jan 29
Jan 31
Feb 02
Feb 04
Feb 06
Feb 08
Feb 10
Feb 12
Date

Figure 6.

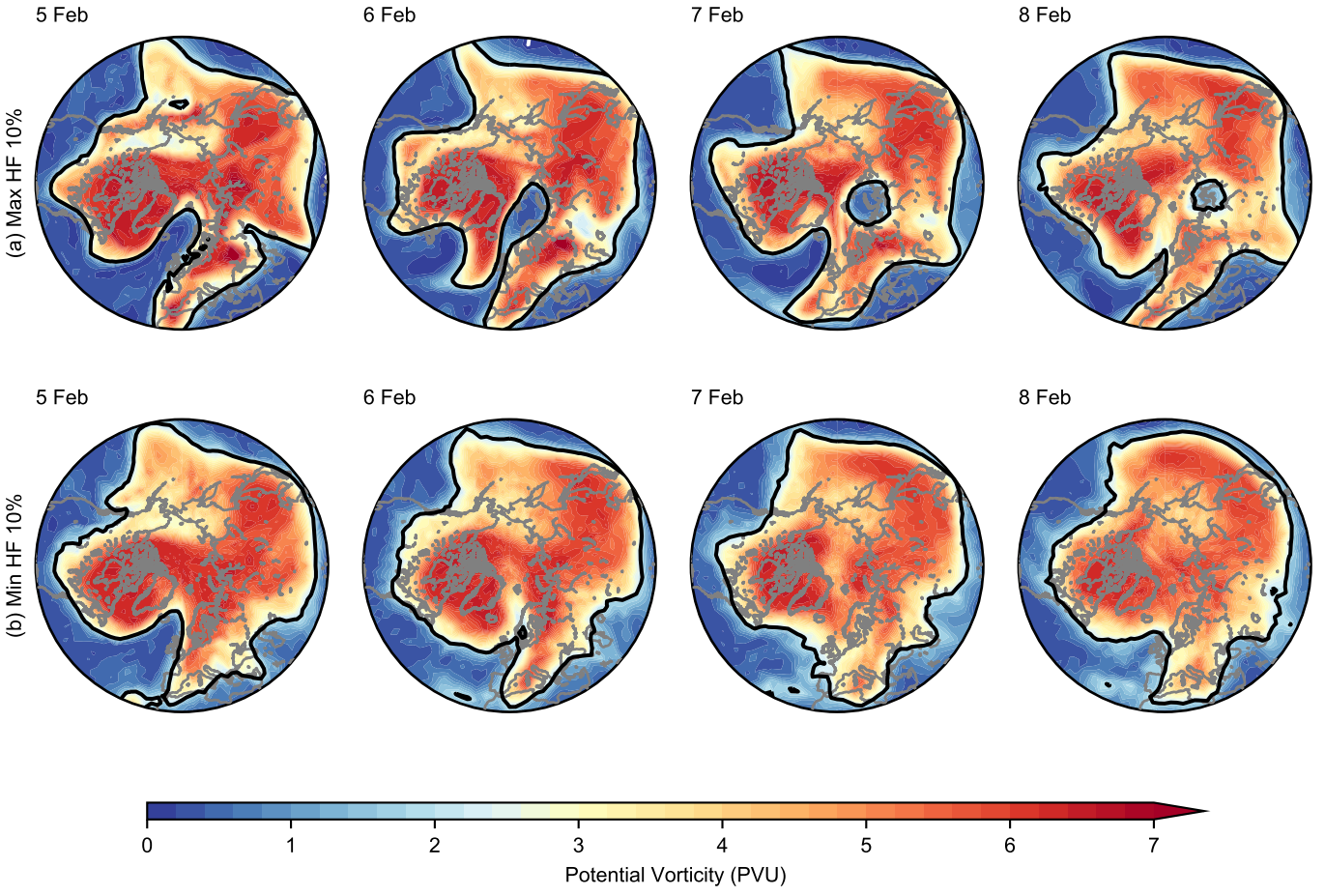
5 Feb
6 Feb
7 Feb
8 Feb
(a) Max HF 10%
5 Feb
6 Feb
7 Feb
8 Feb
(b) Min HF 10%
0
1
2
3
4
5
6
7
Potential Vorticity (PVU)

Figure 7.

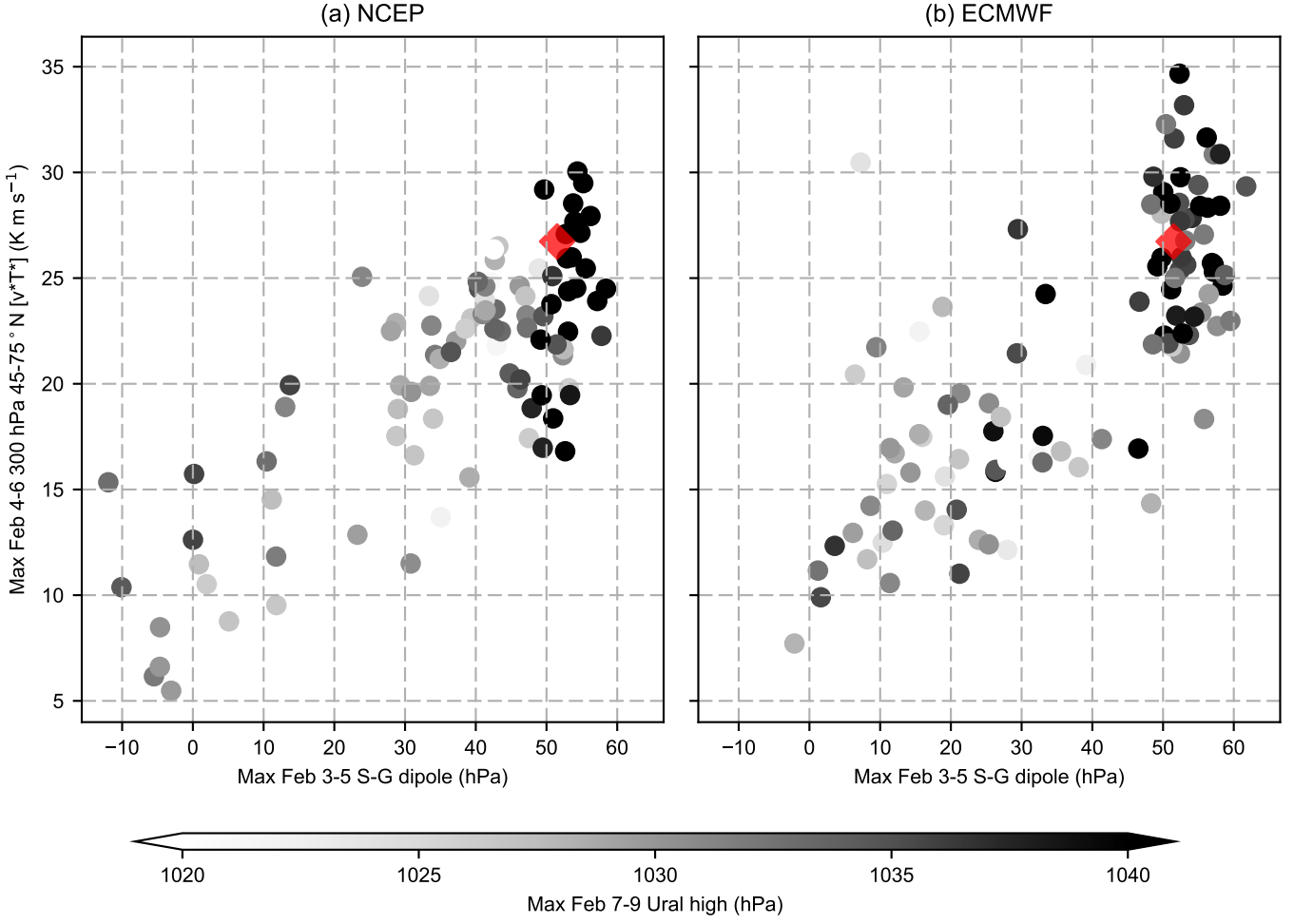
(a) NCEP
(b) ECMWF
Max Feb 4-6 300 hPa 45-75 ° N [v*T*] (K m s^{-1})
Max Feb 3-5 S-G dipole (hPa)
Max Feb 3-5 S-G dipole (hPa)
Max Feb 7-9 Ural high (hPa)
1020
1025
1030
1035
1040

Figure 8.

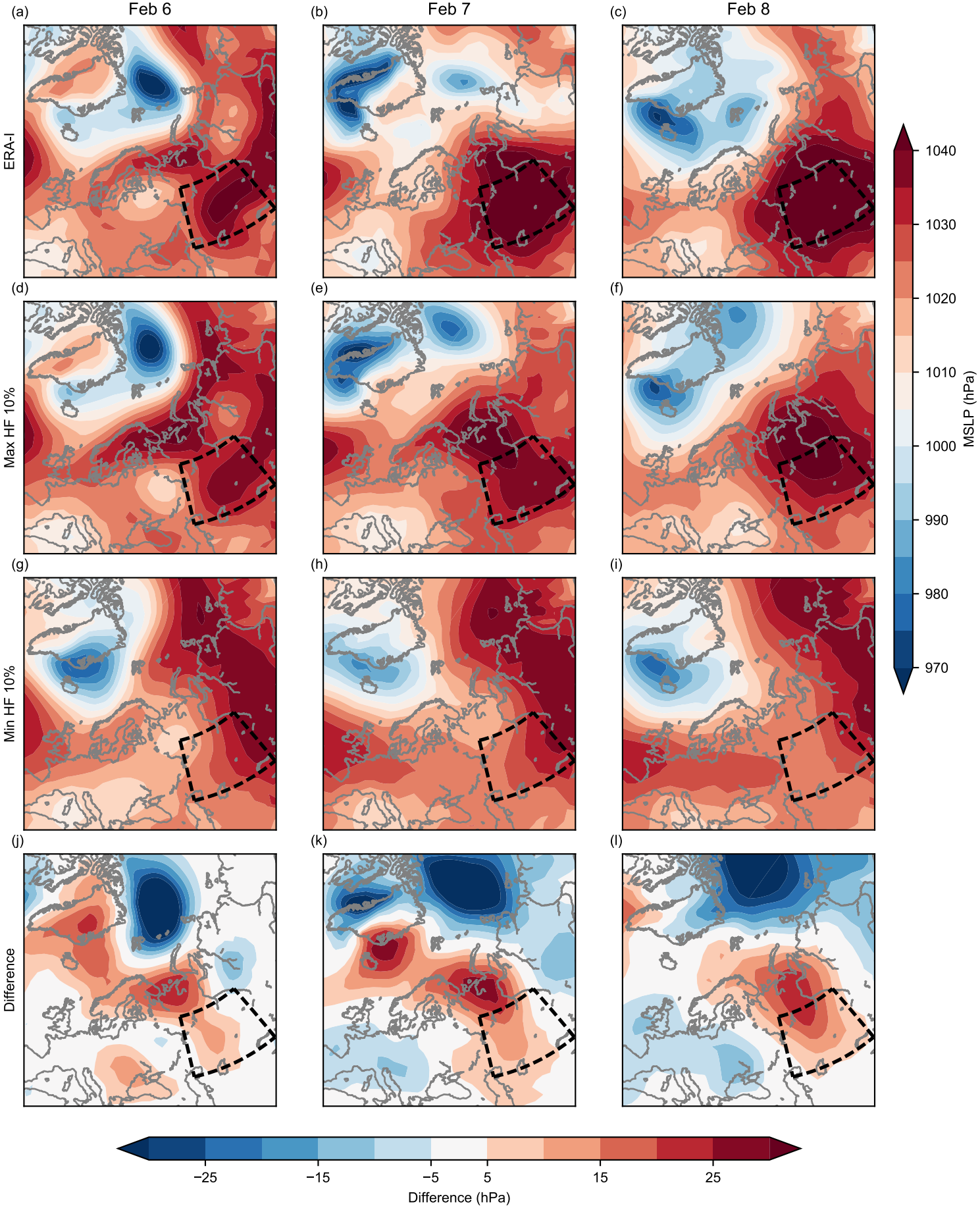
(a)
Feb 6
(b)
Feb 7
(c)
Feb 8
ERA-I
(d)
(e)
(f)
Max HF 10%
(g)
(h)
(i)
Min HF 10%
(j)
(k)
(l)
Difference
1040
1030
1020
1010
1000
990
980
970
MSLP (hPa)
−25
−15
−5
5
15
25
Difference (hPa)

Figure 9.

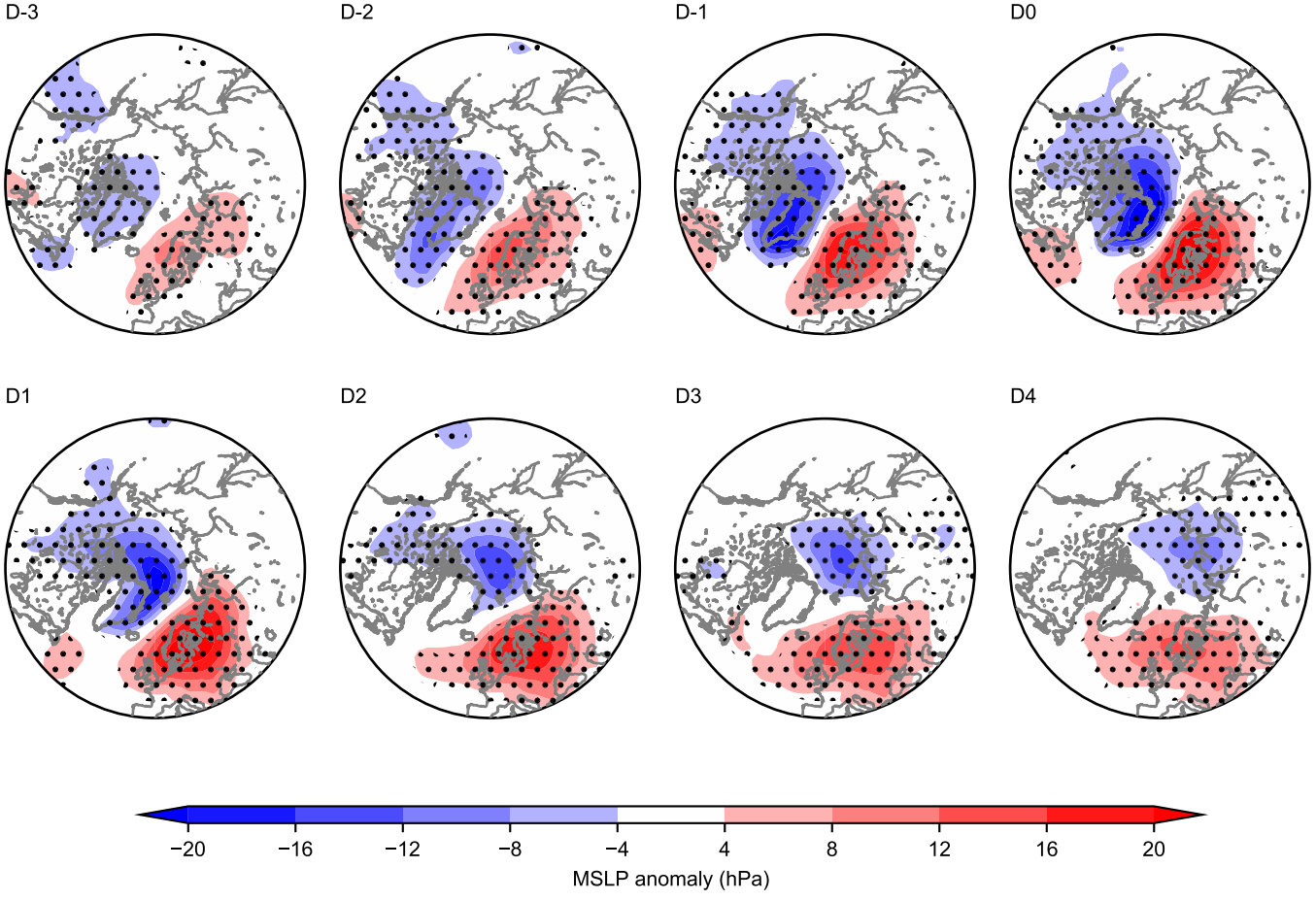
D-3
D-2
D-1
D0
D1
D2
D3
D4
−20
−16
−12
−8
−4
4
8
12
16
20
MSLP anomaly (hPa)

Figure 10.

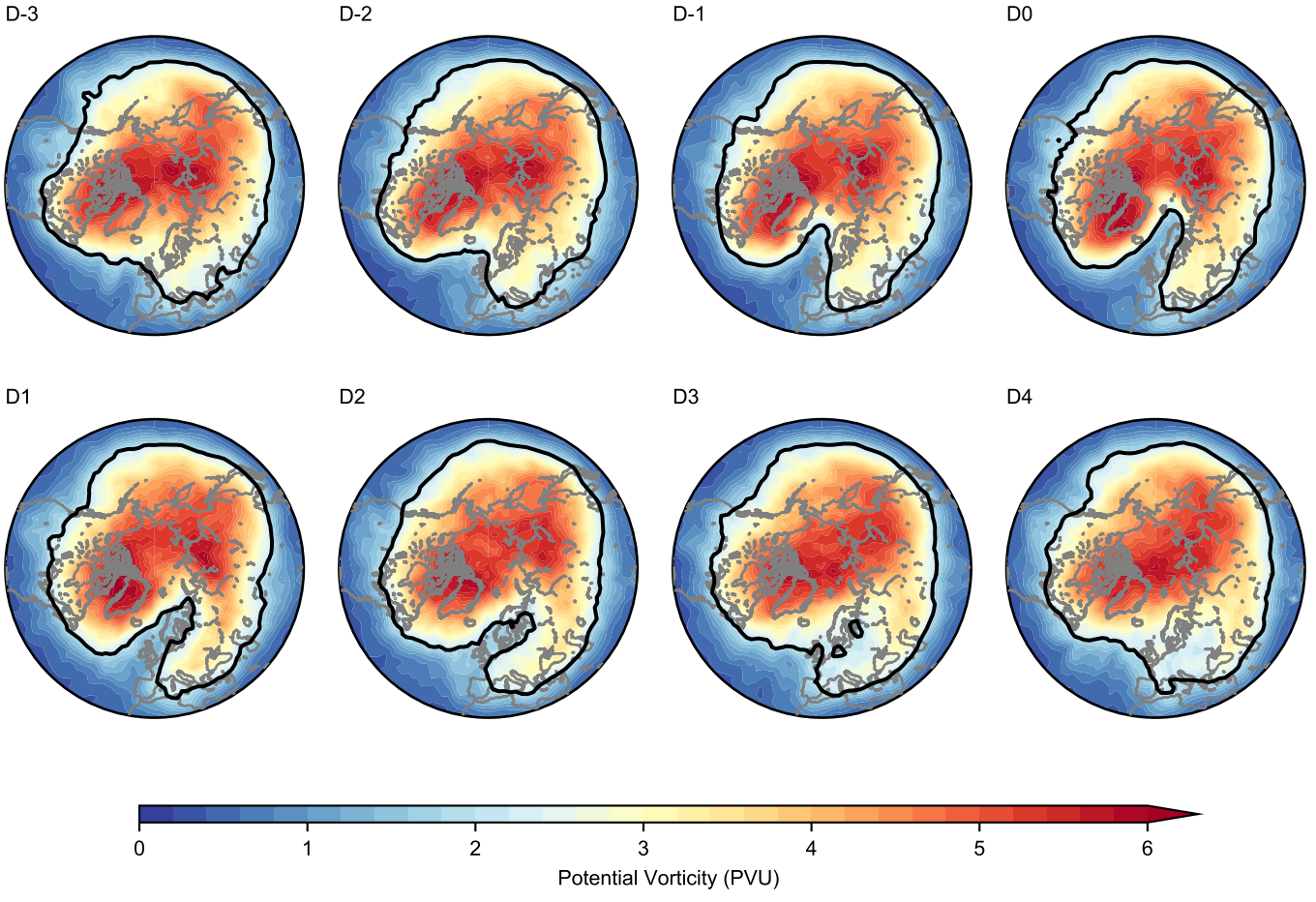
D-3
D-2
D-1
D0
D1
D2
D3
D4
0
1
2
3
4
5
6
Potential Vorticity (PVU)

Figure 11.

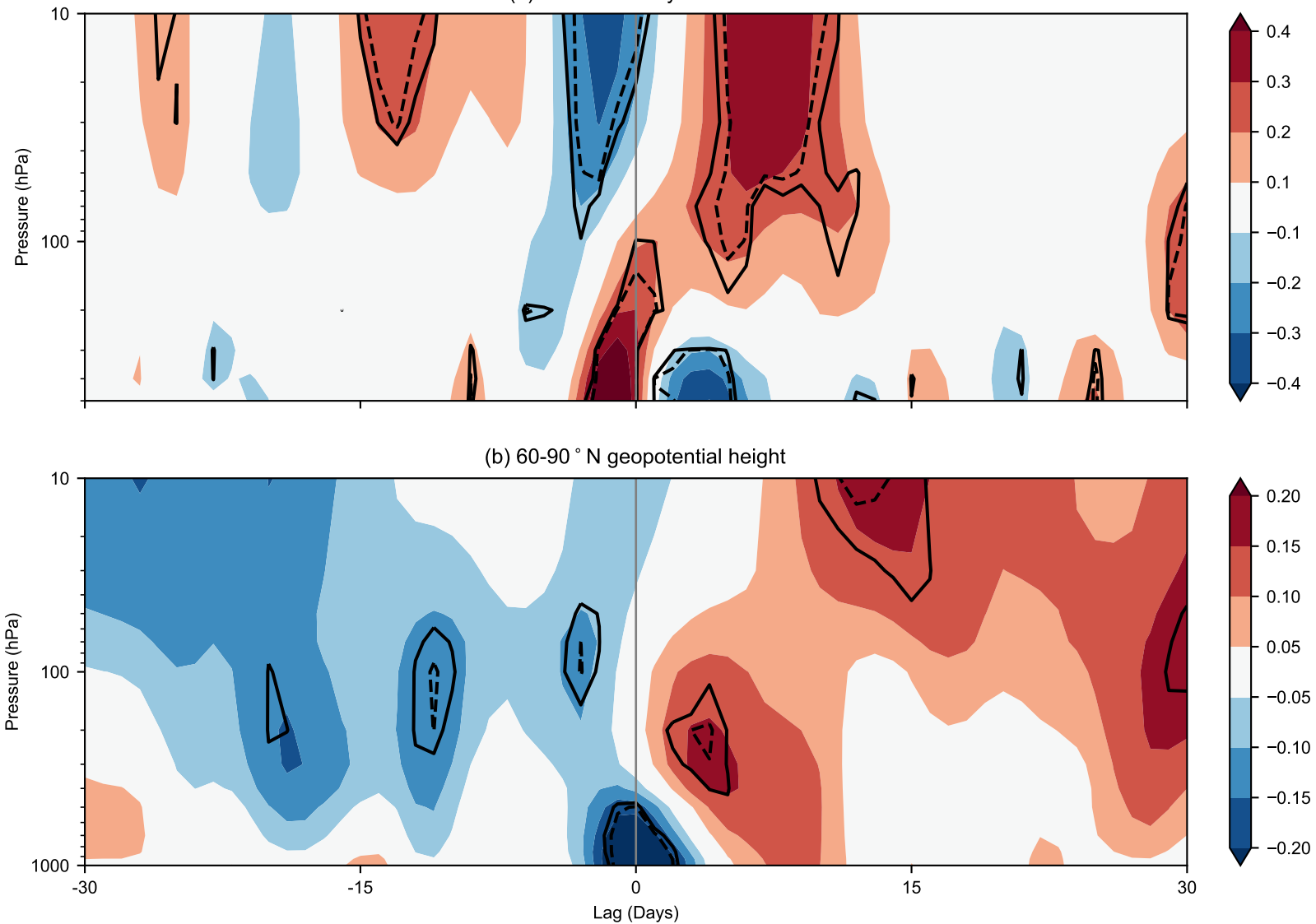
(a) 45-75 ° N eddy heat flux
Pressure (hPa)
10
100
0.4
0.3
0.2
0.1
−0.1
−0.2
−0.3
−0.4
(b) 60-90 ° N geopotential height
Pressure (hPa)
10
100
1000
0.20
0.15
0.10
0.05
−0.05
−0.10
−0.15
−0.20
-30
-15
0
15
30
Lag (Days)